Permanent Magnet Biased Inductors–An Overview

ANDRES REVILLA AGUILAR [1] **(Member, IEEE), STIG MUNK-NIELSEN** [1] **(Member, IEEE),**
FLEMMING BUUS BENDIXEN [2] **(Member, IEEE), ZIWEI OUYANG** [3] **(Senior Member, IEEE),**
MAEVE DUFFY [4] **(Senior Member, IEEE), AND HONGBO ZHAO** [1] **(Member, IEEE)**

[1]Department of Energy, Aalborg Universitet, 9220 Aalborg, Denmark
[2]Buusmag, 9500 Hobro, Denmark
[3]Electro Technology Electronics, Danmarks Tekniske Universitet, 2800 Kgs. Lyngby, Denmark
[4]Power Electronics Research Centre, University of Galway, H91 TK33 Galway, Ireland

CORRESPONDING AUTHOR: HONGBO ZHAO (e-mail: hzh@energy.aau.dk)

ABSTRACT This article provides a comprehensive overview of the state of the art in the field of permanent magnet biased inductors, (PMBIs). The theoretical benefits of PMBIs, operating in DC applications, were identified decades ago, in the late 1950's. Compared with a non-biased inductor, a 100% linear biased PMBI, can achieve the same inductance and saturation current, while requiring only half of the core's cross-sectional area or half the number of turns. In practicality, achieving 100% biasing without introducing additional losses, or detrimental conditions for the permanent magnet's lifetime, becomes an important challenge and the development and achievements of PMBIs have been evolving until present days. Therefore, this overview paper, first introduces the basic background knowledge required for the development of PMBIs, including an overview of the design benefits of biasing, the possible design strategies, additional benefits and possibilities of over-biasing, and a brief introduction to permanent magnets, PMs. The historical evolution of the different biasing techniques, and the employed core and PM topologies, are analyzed and evaluated. The different physical prototype implementations found in the literature, and their operating characteristics, achievements, and limitations, are compiled and evaluated. Finally, the present challenges of PMBI implementation, and the future perspectives towards optimized development are summarized.

INDEX TERMS Pre-magnetized inductors, permanent magnet inductors, biased inductors, hybrid core inductors, magnetic biasing.

I. INTRODUCTION

INDUCTORS and transformers are recognized as one of the main factors limiting the achievable power density of modern electronic converters. Inductors operating in DC applications only utilize the inductance in their positive current range, while their linear inductance in the range of negative currents remains unutilized. Permanent magnet biased inductors, PMBIs can be used to improve the power density of inductors operating in DC applications. The theoretical benefits of PMBIs were identified decades ago during the late 1950s. A 100% biased PMBI can achieve the same inductance and DC saturation as a non-biased inductor, while requiring only 50% of the core's cross-sectional area or number of turns. On the other hand, practically achieving full

biasing of the core becomes an important challenge, due to additional power losses and performance limitations related to the used PM materials. Therefore, the biasing methods, core and PM topologies and their practical achievements have been evolving and improving until the present days. This paper presents an overview of the different PMBI topologies documented in the scientific literature [1], [2], [3], [4], [5], [6], [7], [8], [9], [10], [11], [12], [13], [14], [15], [16], [17], [18], [19], [20], [21], [22], [23], [24], [25], [26], [27], [28], [29], and in patent applications [30], [31], [32], [33], [34], [35], [36], [37], [38], [39], [40], [41], [42], [43], [44], [45], [46], [47], [48], [49], [50], [51], [41], [52], [50], [53], [51], [54], [55], [56], [57], [58], [59], [60], [61], [62], [63], [64], [65], [66], [67], [68], [69], [70], [71], [72], [73], [74]. The
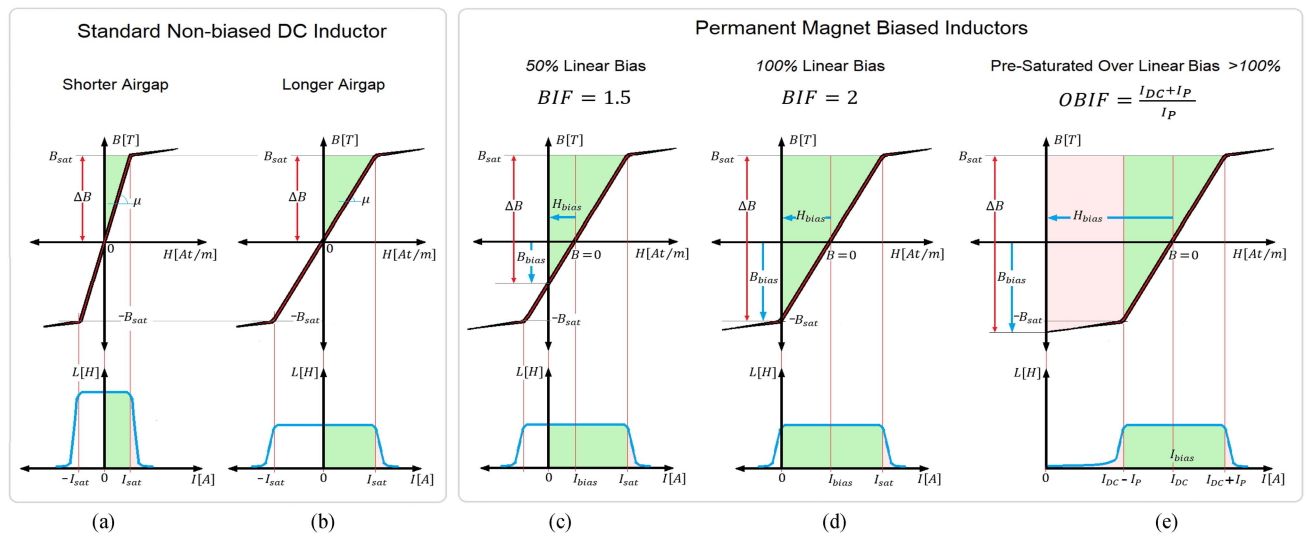
FIGURE 1. BH-loops and inductance vs current profiles of a non-biased DC inductor with (a) shorter airgap and (b) longer airgap. And permanent magnet biased inductors, with (c) 50% linear bias, (d) 100% linear bias, and (e) pre-saturated over >100% linear bias.

technical advantages and limitations and the practical design improvements of the documented PMBI implementations are analyzed and evaluated. The following Section II presents the main and fundamental background knowledge relevant to PMBIs, including an introduction to magnetic biasing, core and permanent magnet materials and a summary of possible design strategies and benefits of magnetic biasing. Section III focuses on the evolution of PMBI topologies, analyzing the main properties, and associated advantages and limitations. Section IV presents a summary of the practical PMBI implementations, documented in the literature, and analyzes their topology and associated design achievements and limitations. The future challenges and perspectives of PMBIs and their possible applications and optimization strategies are introduced in Section V. The final conclusions of the PMBI review are summarized in the latest Section VI.

II. FUNDAMENTAL PMBI KNOWLEDGE
This section presents the theoretical background relevant for the analysis of PMBIs, their possible design strategies and introduction on core and permanent magnet materials.

A. INTRODUCTION TO MAGNETIC BIASING
The saturation limit of ferromagnetic materials is independent of the polarity of the magnetic field within the core, presenting two symmetric saturation flux density limits, B_{sat} and $-B_{sat}$, in the 1st and 3rd quadrants of the BH-loop. Inductor core materials are used as conductors of the magnetic flux, due to their high permeability. On the other hand, the energy storage capacity of common ferromagnetic materials is relatively low, and power inductors typically present an airgap within the length of the core, for energy storage. The airgap length defines the linear inductance value and its associated saturation current. Fig. 1(a) and (b) shows the BH-loop of a theoretical DC inductor and its corresponding inductance versus the

current profile for two airgap lengths. The effective permeability, μ represents the slope of the BH-loop of the inductor, as depicted in Fig. 1(a) and (b). By increasing the airgap length, the saturation current limit is extended, at the expenses of reducing the effective permeability of the inductor, μ and its associated linear inductance value. Independent of the airgap length, the maximum current and inductance product, LI_{max} must remain constant and equal to:

$$L\,I_{max} = B_{sat}\,A_c\,N \qquad (1)$$

Where B_{sat} is the saturation flux density of the core material, A_c is the cross-sectional area of the core and N is the number of turns [75]. In DC applications, the inductor's current and its associated magnetic field strength, H are limited to operate exclusively within the first quadrant and not to reverse polarity into negative current or H values. Thus, the linear inductance region in the 3rd quadrant remains unutilized. PMBIs, present an initial bias magnetization (depicted as blue vectors in Fig. 1), shifting the linear region of the core into the 1st quadrant, and extending the saturation current limit for positive currents. Accordingly, the saturation limit for negative currents has been reduced, and therefore the terminals of PMBIs possess a specific polarity and are only intended to operate in DC inductor applications. Fig. 1(c) and (d) shows the BH-loops, and the associated inductance versus the current curve of two PMBIs, achieving 50% bias and 100% bias respectively. The bias magnetization increases the maximum possible flux density increment, ΔB (depicted by red vectors in Fig. 1) for DC currents. In standard, non-biased DC inductors, the maximum flux density increment, ΔB extends from zero ($0T$) to the core's saturation flux density, B_{sat}. In PMBIs the maximum flux density increment, ΔB_{PMBI} extends from the introduced negative PM bias flux, $-B_{bias}$ (at zero current), to the saturation flux density of the core:
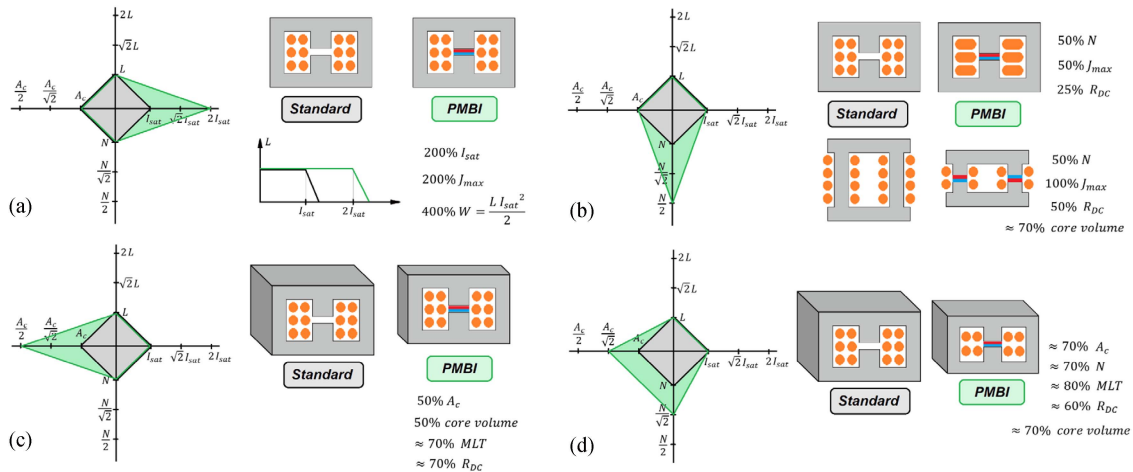
FIGURE 2. Permanent magnet biased inductor's design strategies. Full linear bias (100%) and $BIF = 2$ is assumed. (a) Saturation current, I_{sat} increased by $2x$, (b) number of turns, N reduced by $1/2$, (c) cross-sectional area, A_c reduced by $1/2$, (d) BIF shared between: number of turns, N and cross-sectional area, A_c, resulting in a reduction of $N/\sqrt{2}$ and $A_c/\sqrt{2}$.

- $\Delta B = [0 \quad B_{sat}] = B_{sat}$
- $\Delta B_{PMBI} = [-B_{bias} \quad B_{sat}] = B_{bias} + B_{sat}$

We can define the *Bias Improvement Factor*, *BIF* as the ratio of the maximum flux density increment of the PMBI over the non-biased reference:

$$BIF = \frac{\Delta B_{PMBI}}{\Delta B} = \frac{B_{bias} + B_{sat}}{B_{sat}} \quad (2)$$

and the minimum required current and inductance product, LI_{max} of a PMBI can be expressed by:

$$L\,I_{max\_PMBI} = B_{sat}\,A_c\,N/BIF \quad (3)$$

For achieving 100% linear bias, as in Fig. 1(d), the bias flux density must be equal to the negative saturation limit, $-B_{bias} = -B_{sat}$, and according to (2) then $BIF = 2$. This allows for increasing a factor of *2* times the inductance, L or the saturation current, I_{sat} or reducing by a factor of *1/2* the required cross-sectional area, A_c or the number of turns, N, compared to the non-biased reference. If the bias flux does not reach the negative saturation, $-B_{sat}$ a proportionally lower improvement factor, BIF will be obtained in (2), within the range between *1* and *2*.

B. PRE-SATURATION OVER LINEAR BIASING

Full linear biased PMBIs (as in Fig. 1(d)) concentrate the totality of the linear inductance region into the positive current range (from 0A to I_{max}), allowing for an improvement factor, $BIF = 2$ available for reducing the required LI_{max} product for DC applications (3). In applications where the inductor is operating with a relatively high DC current and a smaller AC *peak-to-peak* current ripple, $I_{DC} \gg I_{PP}$ the inductance is only utilized within a relatively small current range: $(I_{DC} \pm I_P)$. These applications can benefit from *pre-saturation over 100% linear bias* levels. By further concentrating the totality of the linear inductance region into the operating current range (from $I_{DC} - I_P$ to $I_{DC} + I_P$), overbiased PMOBIs can achieve bias

improvement factors larger than two, $BIF > 2$ [22]. In order to introduce bias flux levels higher than $>100\%$ of the linear region of the core, the PMs have to provide an important magnetization force, H_{bias} to bias the core into the negative saturation region, as depicted in Fig. 1(e). At initial conditions of zero current, $I = 0A$ the bias flux is higher than the saturation limit, $B_{bias} > B_{sat}$ and the core is pre-saturated, presenting very low inductance. The linear part of the BH-loop is concentrated on the required current operation range around I_{DC}, and the bias magnetizing force, H_{bias} introduced by the PM, is matched to the DC current operation point.

$$H_{bias} = \frac{N\,I_{DC}}{l_m} \quad (4)$$

Where l_m is the length of the magnetic circuit within the core. The minimally required current and inductance product, LI_{max} of a *PM Over-Biased Inductor*, PMOBI, operating within the current range: $I_{DC} - I_P$ and $I_{DC} + I_P$, as defined in (4) and Fig. 2(e), can be estimated by:

$$LI_{max\_PMOBI} = B_{sat}\,A_c\,N/OBIF \quad (5)$$

Where the *Over-Biasing Improvement Factor, OBIF*, is the ratio of the minimally required current inductance product, LI_{max} of a non-biased inductor (1) and an Over-Biased PMOBI (5), and can be calculated by:

$$OBIF = \frac{LI_{max}}{LI_{max\_PMOBI}} = \frac{I_{DC} + I_P}{I_P} \quad (6)$$

This strategy can result in important size reduction factors, $OBIF \gg 2$ for the required cross-sectional area or number of turns (5), of DC inductors operating with a small current ripple and high DC current, $I_{DC} \gg I_P$ (6).

C. PMBI DESIGN STRATEGIES

The choice for assigning the *BIF* to the possible design variables: L, I, $1/N$ and $1/A_c$, leads to achieving different design benefits. Fig. 2 shows four different examples of design strategies. These design improvements are calculated assuming an ideal EE core PMBI with PM inside the airgap achieving 100% linear bias and $BFI = 2$. Fig. 2(a) shows a PMBI where the *BIF* is used to increase the saturation current, I_{sat}. This results in an equal core size and equal winding DC resistance, while doubling the saturation current, $2I_{sat}$. Applications dominated by copper losses, could benefit from a design strategy utilizing the *BIF* to reduce 50% the number of turns, N, as represented in Fig. 2(b). This strategy could be implemented with two different approaches, as depicted in Fig. 2(b) *(top and bottom)*. If the same window area is used, the wire cross-sectional area could be doubled, $2A_w$ achieving the same window fill factor and only 25% of the reference DC resistance. If the wire's area, A_w is not increased, this strategy results in 50% of the reference DC resistance, and only requires 50% of the total window area, W_a. This is especially advantageous for inductors using single-layer windings, the total length of the core can be reduced, resulting in an additional core volume reduction. Applications benefiting from a reduced inductor weight, could use the strategy depicted in Fig. 2(c), reducing 50% the required core's cross-sectional area, A_c and resulting in an additional reduction of approximately 70% in the *mean length per turn*, *MLT* and the DC resistance of the reference design. Is also possible to distribute the achieved *BFI* between several of the design parameters: L, I, $1/N$ and $1/A_c$. In Fig. 2(d) is depicted a design strategy employing the *BFI* for a reduction of **0.707** for both, the number of turns, $N/\sqrt{2}$ and the core cross-sectional area, $A_c/\sqrt{2}$. This strategy results in approximately 70% core volume, 80% *MLT* and a DC resistance of 60% compared with the non-biased reference.

D. CORE AND PERMANENT MAGNET MATERIALS

The requirement in bias flux, ϕ_{bias} and PM characteristics for PMBIs, are dependent on the saturation flux density of the core material and the frequency of operation. Higher operation frequency requires higher resistivity materials. Fig. 3 shows the more common core and PM materials used for PMBIs. SiFe laminations provide a higher saturation flux density limit and lower resistivity and are commonly used in lower frequency applications (< 1 kHz). Ferrites, MnZn and NiZn provide a relatively lower saturation limit and much higher electrical resistivity, increasing their possible operation frequency (MnZn < 500kHz, NiZn < 3 MHz). Nanocrystalline and amorphous tape cores provide a higher resistivity than SiFe laminations, while presenting a similar saturation limit [90], [91], [92]. Other common core materials like iron powder or SMC, having distributed airgap characteristics, present important challenges for the PM biasing technique, and only small biasing levels have been achieved [17]. PMBIs using core materials with high saturation limit, B_{sat} present a higher
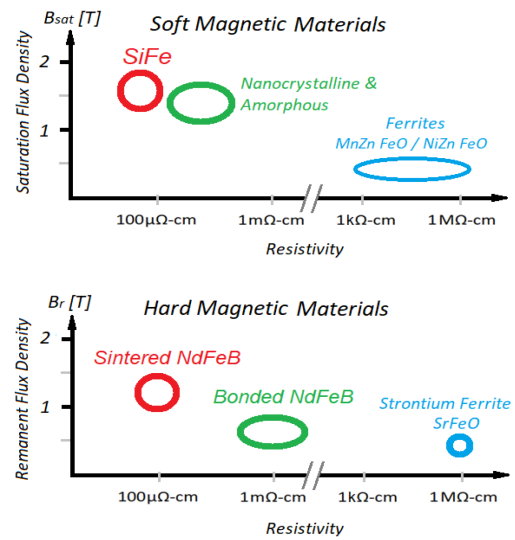

FIGURE 3. Common PMBI's core and PM materials. *Top*: soft magnetic materials for PMBI cores. *Bottom*: hard magnetic materials for PMs. Flux density and electrical resistivity.

demand of bias flux required by the PMs, while lower operation frequency, allows for lower resistivity PM materials. Table I presents a summary of commonly available property ranges among the grades of the different PM materials [79], [80], [81], [82]. Most common NdFeB PMs are typically sintered-NdFeB, achieving the highest energy products, *BH* and a relatively low resistivity. *Strontium-Ferrite*, SrFeO provide the highest resistivity at the expenses of reducing the maximum energy product, *BH*. Bonded-NdFeB provide a compromise of characteristics between sintered-NdFeB and Ferrite PMs. Samarium Cobalt, SmCo achieves lower BH products than NdFeB, while presenting much better thermal performance. The main characteristics of a PM material are described by their demagnetization curves [79], [80], [81], [82], [83]. Fig. 4(a) shows the second quadrant of the demagnetization curves of a generic linear PM. If an opposing demagnetizing force, H_D is applied at the PM's poles, the PM lowers its operation point behaving as a linear source. If the demagnetizing force is stronger than the demagnetization threshold, $H_d > H_K$, characterized by the *knee*, H_K on the *Intrinsic curve*, JH, the PM will be demagnetized. The demagnetization threshold, H_K and all BH characteristics of PMs, are dependent on temperature. To avoid demagnetization of the PMs, the maximum demagnetization field, H_{d_max} at the highest operation temperature must be kept below the associated demagnetization threshold, H_K [81], [82], [83]. Fig. 4(b) shows the demagnetization curves of sintered NdFeB grade N55, at different temperatures [78]. The percentage change in the magnitude of the B_r and H_{cj} values of a PM material, as function of temperature changes, is charactered by the thermal indexes, α and β indicated in Table I [78]. Another important parameter is the cost of the different PM materials. In Table I is indicated the approximate cost of PM material per unit of maximum BH product [79]. Rare earth

TABLE 1. Modern PM Materials Grade Ranges

| PM Material	Br [T]		Hc [kA/m]		Hcj [kA/m]		BH_max [kJ/m³]	Permeability μr	Resistivity ρ [Ω-cm]	Curie Temp. Tc [°C]	Temp.Coef. Br α [%/°C]	Temp.Coef. Hcj β [%/°C]	Cost / BHmax [$ / kJ/m³]
	min	max	min	max	min	max							
Sintered Neodymium. NdFeB	1	1,48	780	915	955	2786	256	1 - 1.1	$150 * 10^{-6}$	310	-0.12	-0.6	1.4 - 3.7
Sintered Samarium Cobalt. SmCo	0.9	1.1	600	800	1200	1830	200	1 - 1.2	$100 * 10^{-6}$	727 - 825	-0.001 -0.045	-0.02 -0.3	12.5
Bonded Neodymium. NdFeB	0.3	0.76	160	517	398	1230	110	1.2 - 1.5	$14 * 10^{-3}$	360	-0.1	-0.4	1.4 - 3.7
Strontium Ferrite.	0.2	0,45	125	288	210	400	24	1.1 - 1.3	$> 10^6$	460	-0.18	+0.4	0.3 - 0.86
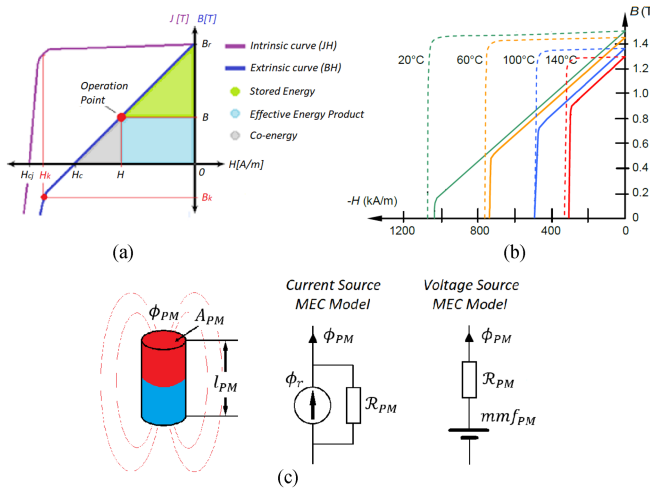
FIGURE 4. Permanent magnets. (a) Generic demagnetization curves, (b) demagnetization curves of sintered NdFeB grade N55 [78], and (c) MEC models of a linear permanent magnet.

materials have a lower availability, and PMs like NdFeB and SmCo, present a higher cost compared to ferrite. Within its linear region, $H_d < H_K$, the PM can be simulated by a linear source *Magnetic Equivalent Circuit*, MEC model, as depicted in Fig. 4(c) [82]. The MEC voltage source model of the PM consists of the ideal voltage source, of value mmf_{PM}, in series with the PM's internal reluctance, $\mathcal{R}_{PM}$, defined as:

$$V_{MEC} = mmf_{PM} = H_c \, l_{PM} \quad (7)$$

$$\mathcal{R}_{PM} = \frac{l_{PM}}{\mu_{PM} A_{PM}} \quad (8)$$

A linear PM can also use a current source model, with an ideal current source equal to the *remanent magnetic flux*, ϕ_r:

$$I_{MEC} = \phi_r = A_{PM} \, B_r \quad (9)$$

The achievable bias flux, ϕ_{bias} is maximized and equal to the remanent flux, $\phi_{bias} = \phi_{PM} = \phi_r$ when the PM's operation point is highest, like in a magnetic short-circuit condition with zero load reluctance, $\mathcal{R}_l = 0$.

III. EVOLUTION OF PERMANENT MAGNET BIASING TOPOLOGIES

Fig. 5(a) to (m) shows a schematic representation of the PMBI topologies documented in the scientific literature [1], [2], [3], [4], [5], [6], [7], [8], [9], [10], [11], [12], [13], [14], [15], [16], [17], [18], [19], [20], [21], [22], [23], [24], [25], [26], [27], [28]. The green vectors are representative of the PM´s flux, ϕ_{PM}. The red vectors represent the magnetic flux introduced by the coils, ϕ_{coil}. The biased core sections present the green and red vectors in opposite directions. The PMBI topologies can be classified into four main types:

- Topologies with PMs inside the airgap.
- Improved topologies with PMs inside the airgap.
- Topologies with PMs outside the airgaps.
- Un-gapped cores biased with a *Saturation-gap*.

The basic MEC models of the main types of PMBI topologies are shown in Fig. 5(o), (p) and (q). Core segments are represented as non-linear resistors with the characteristic BH curve of the core material. The main desired characteristics of an ideal PMBI topology, can be summarized in the following bullet points:

- Maximum allowable PM's area compared to the core's area. $A_{PM} > A_c$. Desirable to maximize achievable bias flux, ϕ_{bias}, and the use of higher resistivity PMs.
- Minimum PM's load reluctance, $\mathcal{R}_l$ to achieve the highest operation point of the PMs, and bias flux, ϕ_{bias}.
- Minimum demagnetizing fields, H_D on PMs. Avoiding demagnetization and maximizing its operation point.
- Minimum EMF's inducing eddy currents on the PMs. Reducing the total AC losses of the PMBI.

Table II presents an evaluation of the different PMBI topologies depicted in Fig. 5 according to the achievable desirable characteristics defined in the previous bullet points.
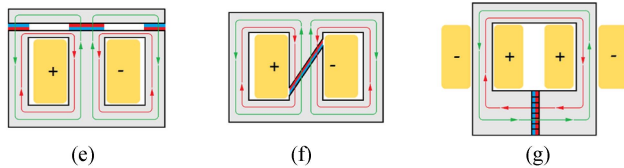
A. TOPOLOGIES WITH PMS INSIDE THE AIRGAPS

The first documented topology utilized standard cores with PMs inside the airgaps [1], [2], [3], [4]. This topology has been implemented with standard *EE*, *UU* or gapped toroid cores, as depicted in Fig. 5(a) to (d) [7], [8], [13], [18], [19], [20], [22], [23], [24]. The maximum allowable PM's area is limited by the core's cross-sectional area, $A_{PM} \leq A_c$. If the
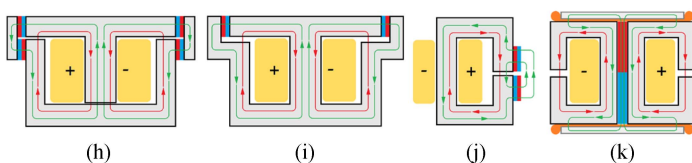
Permanent Magnets inside the airgap
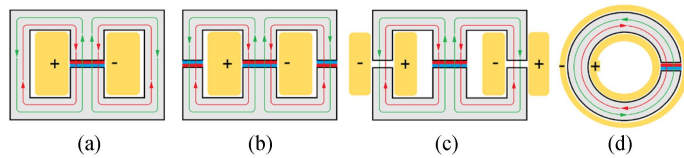
Improvements with Permanent Magnets inside the airgap

Permanent Magnets outside the airgaps
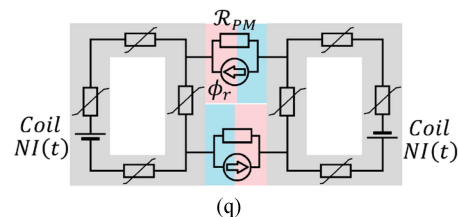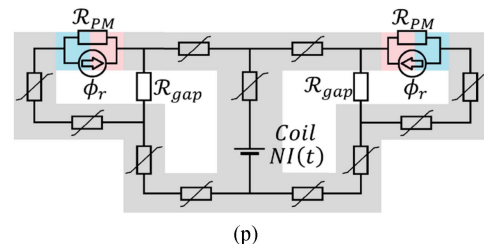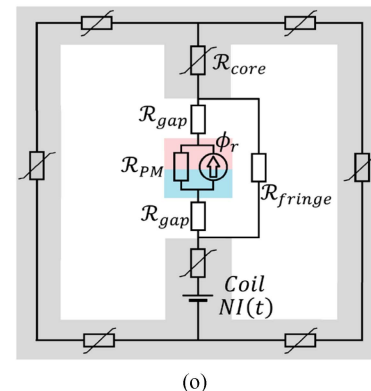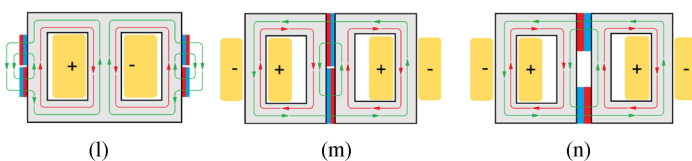
Ungapped Cores with Saturation-gap

FIGURE 5. Permanent magnet biased inductor, PMBI topologies. Red vectors represent magnetic flux introduced by coils. Green vectors represent the PM's magnetic flux. Coil windings in yellow, "+" sign indicate current *into the page*, and "-" sign is current *out of the page*.

TABLE 2. Characteristics Evaluation of PMBI Topologies From Fig. 5

Topology	Topologies with PM inside air-gap				Improved Topologies with PM inside air-gap			Topologies with PM outside the air-gap				The Saturation-gap		
	a)	b)	c)	d)	e)	f)	g)	h)	i)	j)	k)	l)	m)	n)
Allowable PM area	Fair	Fair	Fair	Fair	Fair	High	High	Fair	Fair	High	Low	High	High	High
Operation point of PMs	Fair	Fair	Fair	Fair	High	High	High	Fair	High	Low	High	Low	High	High
Demagnetization Filed on PMs	Strong	Strong	Strong	Strong	Fair	Fair	Fair	Good	Good	Good	Good	Good	Good	Good
EMFs in PMs (Induction of Eddy-Currents)	Strong	Strong	Strong	Strong	Fair	Strong	Strong	Good	Good	Good	Fair	Good	Good	Good

PM is completely filling the length of the airgap, the PMs load reluctance, is equal to the reluctance of the core, and can be considered a magnetic short-circuit, achieving a high operation point of the PM. On the other hand, the PM is subject to strong demagnetizing fields. If the coil's field is stronger than the demagnetization threshold, $H_d > H_K$, the PM will be damaged. A common strategy to reduce the demagnetization field, H_d is to use a PM with the length shorter than the airgap length, creating smaller airgaps around the

PM. Fig. 5(o) shows the MEC model of a PMBI using this topology. The airgaps between the PM and the core introduce an additional fringe reluctance around the PM, and successfully reduce the demagnetization field. The airgaps between the PM and core gap endings increase the load reluctance of the PM, reducing its operation point and achievable bias flux. Fringing flux from the airgap also increases AC copper losses, especially in high-frequency applications [104]. PMs inside the airgap are subjected to all the coil's magnetic flux
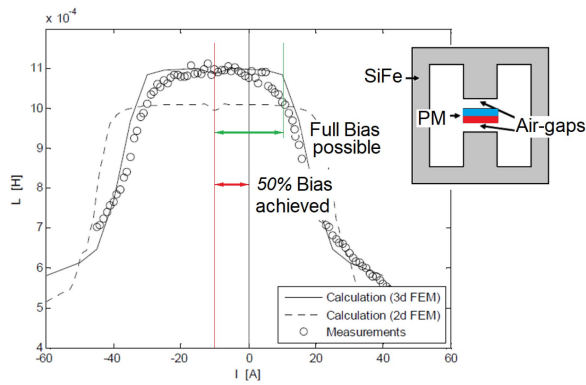
FIGURE 6. PMBI with PM inside the airgap. Inductance vs current, *L vs I*, measured and calculated with 2D and 3D FEM [8].
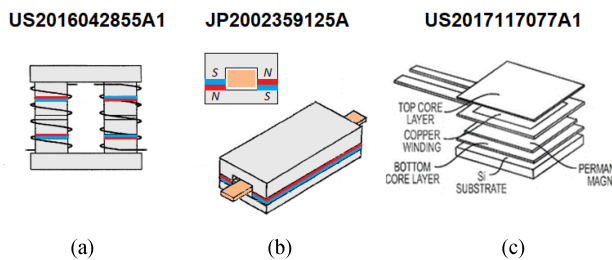

| (a) | (b) | (c) |

FIGURE 7. PMBI patents with PMs inside the airgaps. (a) UU core with multiple PMs in series [68], (b) single winding biased inductance [40], and (c) planar PMBI for on-chip inductors [70].

FIGURE 8. PMBI patents with PMs outside the airgaps. (a) Single EI cores [37]. (b) [65] and (c) [69] using pairs of UU cores, with PMs near the airgaps. Red vectors represent magnetic flux introduced by coils. Green vectors represent the PM's magnetic flux.

fluctuations, inducing eddy currents. Several patents have been found employing very similar topologies with PMs inside the airgap, [33], [34], [35], [39], [40], [41], [42], [43], [44], [45], [46], [47], [48], [49], [51], [54], [56], [57], [58], [61], [64], [68], [70]. Fig. 7 presents some of the patented PMBIs employing PMs inside the airgaps. In Fig. 7(a) is presented a patented PMBI using a ferrite UU core and single-layer windings [68]. The UU cores present several PMs in a series of distributed airgaps. This strategy can reduce the total demagnetization field in each magnet, as compared with a single PM and airgap. The benefits of using distributed series PMs inside distributed airgaps, have been further extended to the development of a pre-biased compound material, as described in the patent [74], consisting of soft and hard ferromagnetic layers, presenting 50% higher saturation current, compared with similar non-biased material. Other trends found in PMBI patent documents focus on the development of biased planar inductors, and distributed micro-inductors, for on-chip applications [100], [101], [102]. Fig. 7(b) presents a PM-biased ferrite core designed for a single winding inductance element, suitable for integrated inductance designs and PCB-micro-inductors [40]. Fig. 7(c) presents a PMBI patent using a planar core with PMs in the airgap between the core plates and the planar copper windings [70].

B. IMPROVEMENTS OVER PMS INSIDE THE AIRGAPS

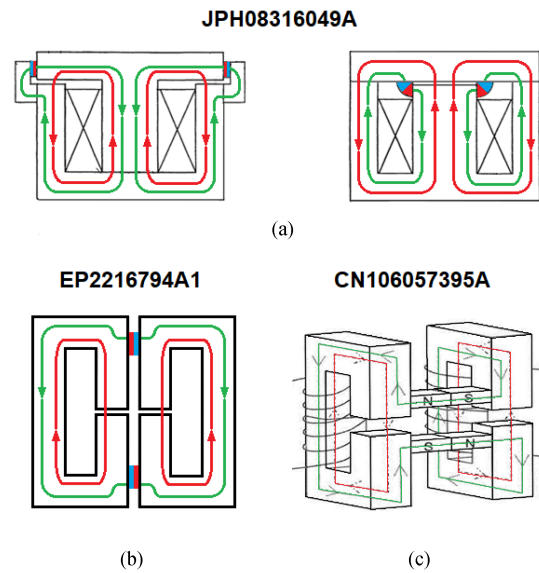Fig. 5(e) presents the topology used by the first PMBI product available in the market, developed by TDK in 1982. It uses a ferrite core with small saturable segments between the PM and the coil, greatly reducing demagnetization fields on the PM [5]. The authors of the first publications on PMBIs using PMs inside the airgap [1], [2], [3], [4], also introduced the idea of using *angled airgaps* as depicted in Fig. 5(f). This geometry can increase the maximum achievable PM's area, while reducing the demagnetization field induced on the PM. This topology requires non-standard core shapes, and no physical implementations have been documented. The topology depicted in Fig. 5(g) employs a *UU* core, presenting the PM inside the airgap [23]. The PM is in a core segment with an increased area, allowing for an increased PMs area, at the expense of a volume increment of one of the core segments. The bigger PM area increases the achievable bias flux level, compared with the basic topology in Fig. 5(a) to (c).

C. TOPOLOGIES WITH PMS OUTSIDE THE AIRGAPS

To reduce the demagnetizing fields on the PMs, a common strategy used by some PMBI topologies has been to place the PMs outside the airgaps, as depicted in Fig. 5(h) to (k). These topologies typically require non-standard core shapes or additional segments of ferromagnetic materials for guiding the PM's bias flux. The additional segments contribute to the total volume. The core segments near the airgaps would also present a reduced effective area, due to the partial saturation induced by the PMs, as documented in [27]. The maximum allowable PM's area in both topologies depicted in Fig. 5(h) and (i), is limited by the core's cross-sectional area, $A_{PM} \leq A_c$. Very similar topologies to Fig. 5(h) and (i), have also been found in patent documents [36], [37], [38], [50], [51], [55], [59], [60], [62], [63], [65], [66], [67], [69], [71], [72]. In Fig. 8(a) [37] is depicted a PMBI topology using modified

EI cores, and the possibility of using standard EI cores with special PMs, presenting a 90° angle between its magnetization poles. In Fig. 5(j) is depicted a topology employing *UU* cores with PMs in the vicinity of the airgap, allowing for an increased PM's cross-sectional area. This topology does not use any additional core segment to contain the biasing flux on the back between the PMs, and therefore the PM operation point, and the achieved bias are limited. Similar topologies have also been found in patent documents [65], [69], as depicted in Fig. 8(b) and (c), presenting a pair of special UU cores, with airgaps, and biased by the same pair of PMs near their airgaps. This configuration minimizes the PMs load reluctance and maximizes the achievable bias. On the other hand, UU cores with a single airgap in only one of their legs, can present mechanical challenges. The latest documented PMBI topology using PMs outside the airgap, was developed at *M.I.T.* in 2022 [25]. This topology, depicted in Fig. 6(k), employs a ferrite pot-core with a long PM inserted into the hollow central pole. The PM's flux is guided to the edges of the pot-core with the use of additional plates of soft magnetic material, *Hiperco-50*. The maximum allowable PM's area is limited by the dimensions of the hole in the central pole of the ferrite pot-core. The PM's area is smaller than the effective cross-sectional area of the core, $A_{PM} < A_c$. The PM inside the hollow central pole does not contribute to flux variations and the associated EMFs induced by the coil, since the flux will concentrate on the higher permeability ferrite. On the other hand, the *Hiperco-50* plates present a permeability higher than ferrite and much lower resistivity, and strong EMFs will be induced. This topology employed a "ring-shield" (shown in orange in Fig. 5(k) and Fig. 12.) to reduce eddy losses in the *Hiperco-50* plates [25].

D. THE SATURATION-GAP BIASING TOPOLOGY

This topology employs standard *EE* or *UU* cores with no airgaps, as depicted in Fig. 5(l), (m) and (n) and the MEC model in Fig. 5(q). Part of the PM's flux will flow through the longer section of the core, in the opposite direction to the coil's flux and provide the desired bias magnetization. In the smaller portion of the core between the PMs, the magnetic flux from both the coil and the PMs presents the same polarity, becoming partially saturated and presenting the equivalent reluctance of a typical airgap. This section of the core is referred to as the *saturation-gap*, and its reluctance is proportional to the reluctance of the PMs [14], [15], [16], [21]. The PM's area is not limited by the core's cross-sectional area, and the PMs outside the core present minimal demagnetization fields. The optimized Saturation-gap topologies depicted in Fig. 5(m) and (n), consist of two standard UU cores with no airgaps, simultaneously biased by the same pair of PMs. In these topologies, the PMs are placed in a *short-circuit* condition, optimizing their operation point and the achievable bias flux.
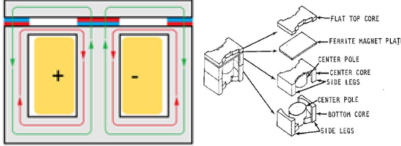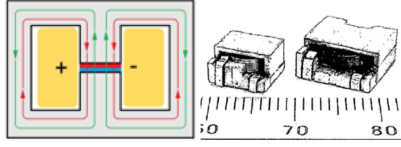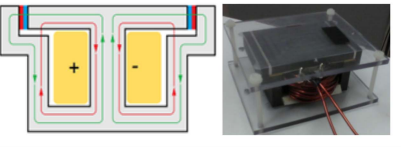
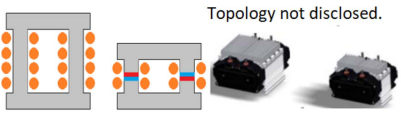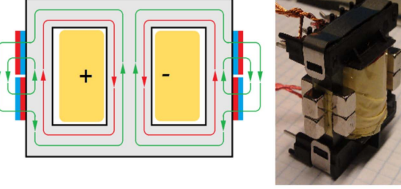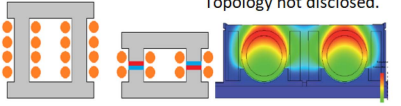## IV. PRACTICAL PMBI IMPLEMENTATIONS

Several PMBI prototypes employing the topologies presented in Fig. 5, and using the different cores and PM materials, have

been documented in the literature [5], [6], [7], [8], [9], [10], [11], [12], [13], [14], [15], [16], [17], [18], [19], [20], [21], [22], [23], [24], [25], [26].

A. PMBI IMPLEMENTATIONS USING FERRITE CORES

Ferrite core materials have been the first and most common choice for the investigation and development of PMBIs. Due to their relatively lower saturation flux density, B_{sat} the bias flux requirement, ϕ_{bias}, are more easily achieved. A total of twelve different PMBI implementations using ferrite cores have been documented. Table III present a summary of the different PMBI implementations, the topology employed, materials, electrical characteristics, and their achieved bias flux, *BFI*, and overall design benefits. Only three PMBIs have been found as commercial products available in the market. The first PMBI product was the *PCH Core*, developed by *TDK* using the topology depicted in Fig. 5(e) and published in 1982 [5]. The used PM material was Barium Ferrite, with a relatively low remanent flux density, B_r. This topology achieved 30% bias flux, and 30% higher saturation current. The second commercially available PMBI product was developed by STS in 2014 [13]. This PMBI is marketed as MaxFlux and can achieve 100% bias of ferrite cores. The PM and core topology is not disclosed in [13]. The third and latest PMBI product available on the market, was developed by SUMIDA Electronics in 2015 [18]. The specific topology and PM placement are also not disclosed. The topologies of these two PMBI products [13], [18], probably employ PMs inside airgaps, or a combination of hard PM material filled inside a distributed airgap, as described in patent [73]. A patent document by STS documents a UU core with a multitude of PMs in series distributed airgaps, as depicted in Fig. 7(a) [67]. The first PMBI prototype using the basic topology with PMs inside the airgap was implemented for a miniaturization of a flyback transformer for a PC power supply in 2003 [7]. This study compared two different types of PMs: standard sintered NdFeB PMs and bonded NdFeB PMs. Sintered PMs presented important eddy current losses, and the use of bonded PMs was the preferred choice, providing a higher resistivity, while lower remanent flux density, B_r. The use of higher resistivity bonded PMs achieved an almost identical Q factor as the non-biased reference, at the expense of achieving a lower bias level. This implementation achieved 60% bias flux and reduced the core's cross-sectional area and the total core volume by a 30%. Four implementations have been documented achieving 100% bias of ferrite cores, using sintered NdFeB PMs, with different topologies [11], [14], [20], [22]. In [20] is also presented an FEA simulation of the demagnetization field of the PM, which assures that the fields are below the demagnetization threshold. Sintered PMs provide the highest coercive force and bias flux, at the expenses of presenting a relatively low resistivity. The AC losses, in these PMBI implementations, are significantly increased, and can only operate in applications at a relatively low frequency or small current ripple, $I_{PP} \ll I_{DC}$. Another PMBI prototype was documented in 2019 [24], using the basic topology with PMs inside the
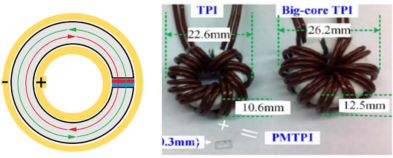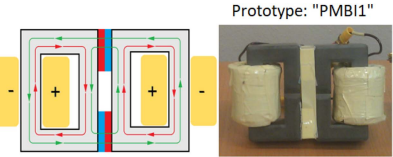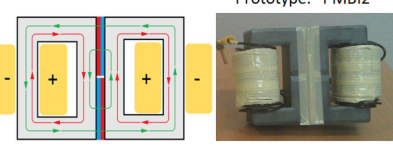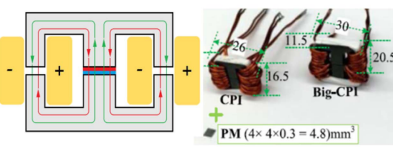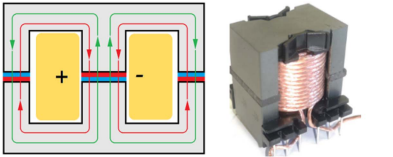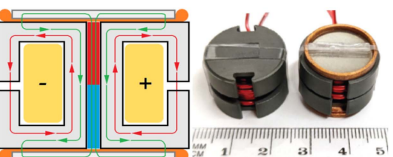
TABLE 3. Physical PMBI Implementations Using Ferrite Cores. *Part 1-of-2, From 1982 to 2015*

Ref. Nr.	Publication Title PMBI Topology / Implementation	Year	Core material	PM material	Electrical Specifications	Bias % $BIF = \frac{B_{bias}+B_{sat}}{B_{sat}}$	Design Strategy Achievements
[5]	TDK PCH Core "A new reverse-biased choke coil"	1982	Ferrite TDK H7C1 Bsat 0.4 T ρ >1 kΩ-cm μr 10000	Barium Ferrite TDK FB3B Br 0.34 T ρ >1 MΩ-cm μr 1.2	Different models Frq max 200 kHz L max 1.5 mH IDC max 36 A Ipp max 36 A	30% BIF = 1.3	Comparison with equivalent core size. 30% higher saturation current. 70% higher Energy Density. 30% more inductance below 10% load current.
[7]	"A new downsized large current choke coil with magnet bias method"	2003	MnZn Ferrite FEY28 Bsat 0.4 T ρ > 1 kΩ-cm μr 8000	Bonded NdFeB Br 0.16 T ρ > 10 kΩ-cm μr 1.2	Frq 100 kHz L 0.7 uH IDC 23 A Ipp Not specified	60% BIF = 1.6	Comparison with equivalent inductance and saturation current. 32% less core volume Equivalent DC resistance.
[11]	"Design Paradigm for permanent-magnet-inductor-based power converters"	2013	Ferrite 3F3 Bsat 0.35 T ρ 200 Ω-cm μr 4000	Sintered NdFeB N38SH Br 1.2 T ρ 150 μΩ-cm μr 1	Frq 17 kHz L 3 mH IDC 20 A Ipp 3 A	Not Specified ≈ 100% BIF ≈ 2	Comparison with equivalent inductance and saturation current. 40% total mass reduction.
[13]	STS "MaxFlux–Magnetically Biased Inductor" Topology not disclosed.	2014	Ferrite STS propietary Bsat Not specified ρ Not specified μr Not specified	Not disclosed STS proprietary Br Not specified ρ Not specified μr Not specified	Frq 16 kHz L 75 uH IDC 300 A Ipp 120 A	100% BIF = 2	Comparison with equivalent inductance and saturation current. 50% less number of turns. 50% lower DC resistance. 41% less total mass.
[14]	"Method for introducing bias magnetization in ungaped cores, The Saturation-gap"	2014	MnZn Ferrite N87 Bsat 0.49 T ρ > 1 kΩ-cm μr 2200	Sintered NdFeB N42 Br 1.2 T ρ 150 μΩ-cm μr 1.1	Frq 8 kHz L 340 μH IDC max 5 A Ipp max 10 A	Prototype PMI1. Two pairs of PMs per leg. 100% BIF = 2 Prototype PMI2. Three pairs of PMs per leg. >100% BIF = 3	100% higher saturation current. Identical DC resistance. Over linear bias. 200% higher saturation current. Identical DC resistance.
[18]	SUMIDA "Magnetically Biased High Power Coil Module" Topology not disclosed.	2015	MnZn Ferrite Fi399 Bsat 0.5 T ρ > 1 kΩ-cm μr 1200	Sintered NdFeB N38SH Br Not specified ρ Not specified μr Not specified	Frq 72 kHz L 5 μH IDC 55 A Ipp Not specified	75% BIF = 1.75	Comparison with equivalent inductance and saturation current. 42% less number of turns. 42% lower DC resistance. 28% less core volume. volume.

airgaps depicted in Fig. 5(b). This prototype employed ferrite cores and bonded NdFeB PMs. The higher resistivity of bonded PMs greatly reduces eddy currents compared to sintered PMs. In this PMBI, the airgaps are filled by the PMs, and it achieves 100% bias which doubles the saturation current,

from $I_{sat} = 14\,A$ to $2I_{sat} = 28\,A$. Bonded PMs present a lower demagnetization threshold compared with sintered PMs, and the expected fields on the PMs, with no fringing airgaps, could be higher than the threshold of demagnetization. The prototype is tested on a DC-AC inverter operating quite below

TABLE 3. *(Continued.)* Physical PMBI Implementations Using Ferrite Cores. *Part 2-of-2, From 2015 to 2022*

| Ref. Nr.	Publication Title PMBI Topology / Implementation	Year	Core material	PM material	Electrical Specifications	Bias % $BIF = \frac{B_{bias}+B_{sat}}{B_{sat}}$	Design Strategy Achievements
[20]	"Evaluation of High-Current Toroid Power Inductor With NdFeB Magnet for DC–DC Power Converters"	2015	Ferrite 3C20 Bsat 0.35 T ρ 500 Ω-cm μr 5500	Sintered NdFeB N35EH Br 1.06 T ρ 180 μΩ-cm μr 1	Frq 300 kHz L 7 μH IDC 14 A Ipp 0.6 A	100% BIF = 2	Comparison with equivalent inductance and saturation current. 40% less core volume. Equivalent DC resistance.
[21]	"Half Size Reduction of DC Output Filter Inductors with the *Saturation-gap* Magnetic Bias Topology" Prototype: "PMBI1"	2016	MnZn Ferrite MF198A Bsat 0.47 T ρ > 500 Ω-cm μr 5500	Bonded NdFeB Br 0.8 T ρ 20 mΩ-cm μr 1.5	Frq 30 kHz L 5 mH IDC 9 A Ipp 2 A	100% BIF = 2	Compared with equivalent inductance and saturation current. 50% smaller core area cross-section. 50% less core volume. 16% lower DC resistance
[21]	"Half Size Reduction of DC Output Filter Inductors with the *Saturation-gap* Magnetic Bias Topology" Prototype: "PMBI2"	2016	MnZn Ferrite Fi399 Bsat 0.47 T ρ > 500 Ω-cm μr 5500	Bonded NdFeB Br 0.8 T ρ 20 mΩ-cm μr 1.5	Frq 30 kHz L 5 mH IDC 9 A Ipp 2 A	>100% BIF = 3	Compared with equivalent inductance and saturation current. Over linear bias. 50% smaller core area cross-section. 50% less core volume. 35% less number of turns. 50% lower DC resistance. 50% total volume.
[22]	"Permanent-Magnet Coupled Power Inductor for Multiphase DC–DC Power Converters"	2017	Ferrite N87 Bsat 0.45 T ρ 1000 Ω-cm μr 2200	Sintered NdFeB N35EH Br 1.06 T ρ 180 μΩ-cm μr 1	Frq 150 kHz L 4 μH IDC 22 A Ipp 0.5 A	92% BIF = 1.92	Comparison with the same inductor without PMs. 92% higher saturation current. 48% core volume reduction compared to standard non-biased coupled inductors.
[24]	"Premagnetized Inductors in Single Phase dc-ac and ac-dc Converters"	2019	Ferrite (grade not specified) Bsat ≈ 0.45 T ρ ≈ 1 kΩ-cm μr ≈ 3000	Bonded NdFeB Br 0.46 T ρ 20 mΩ-cm μr 1.2	Frq 400 kHz L 240 μH IDC 5 A Ipp 2 A Isat 28 A	100% BIF = 2	Comparison with the same inductor without PMs. 100% higher saturation current. Equivalent DC resistance.
[25]	"Permanent Magnet Hybrid Core Inductors for High Saturation Capability"	2022	Ferrite 3F46 Bsat 0.52 T ρ 500 Ω-cm μr 1500 Hiperco-50 Bsat 2.3 T ρ 40 μΩ-cm μr 15000	Sintered NdFeB N40SH Br 1.28 T ρ 150 μΩ-cm μr 1	Frq 1 MHz L 35 μH IDC 10 A Ipp Not specified	45% BIF = 1.45	Comparison with the same core volume, inductance and saturation current. 27% less number of turns. 50% lower DC resistance.
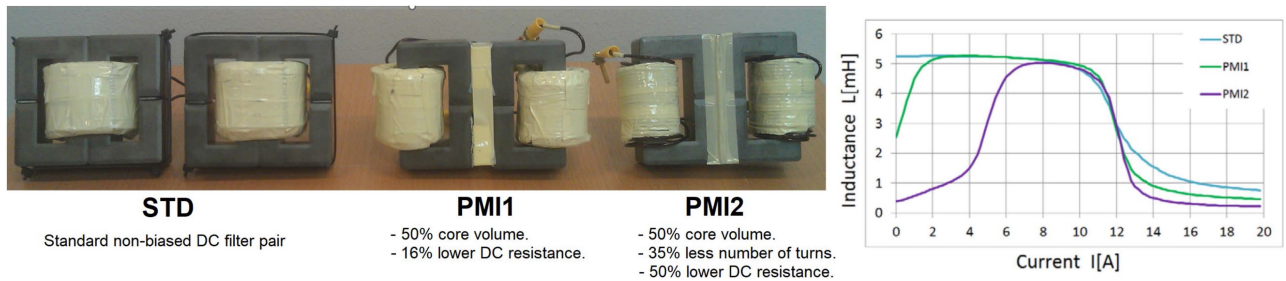
FIGURE 9. Implemented DC filter pairs. STD, is standard non-biased filter *EE* inductor pair. PMI1, is 100% PM biased *UU* inductor pair. PMI2, is >100% pre-saturated over linear bias, *UU* inductor pair. *Right*: Measured inductance vs current profiles, *L vs I* of the three filters. Each filter contains two inductors in series. Data from [21].
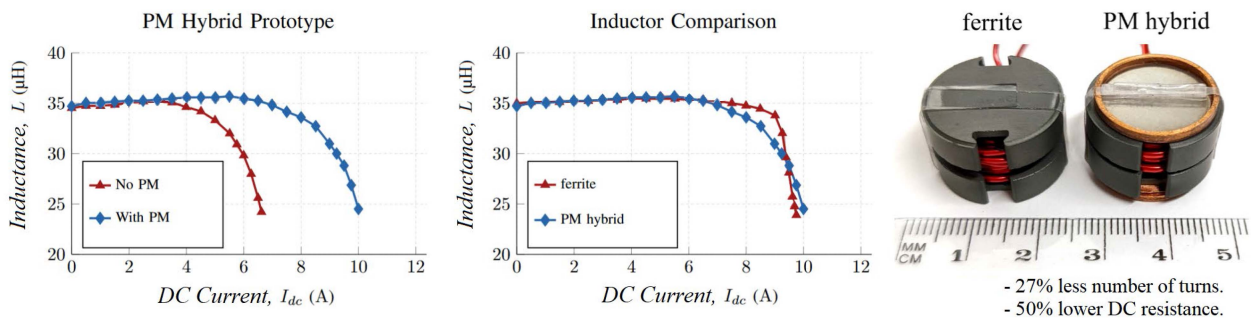

FIGURE 10. Measured inductance versus current, *L vs I* profiles. *Left*: *L vs I* of PMBI prototype (PM Hybrid) with and without PM. *Center*: *L vs I* of PM-Hybrid and non-biased ferrite core with same inductance and saturation. *Right*: Implemented prototypes. Non-biased ferrite core uses bobbin with 15 turns and PM-Hybrid uses 11 turns. Data from [25].

its saturation limit, with a *50 Hz* AC current of $I_{rms} = 5\ A$ with a *400 kHz* current ripple with $I_{PP} = 2\ A$. The Saturation-gap topology, as depicted in Fig. 5(m) and (n), has been implemented using ferrite cores and bonded-NdFeB PMs [21]. The two *UU* PMBIs connected in series, are compared with two standard non-biased EE core inductors, operating in a DC-DC converter, at *36 kHz* switching frequency, with $I_{DC} = 9A$ and a current ripple of $I_{PP} = 2A$. Two different prototypes were implemented achieving the same inductance within the current operation range, with 100% bias and Over-Bias flux levels. PMI1 achieves full linear 100% bias, and the $BIF = 2$ is employed to reduce the core cross-sectional area by 50%. By reducing the core's area, the mean length per turn, *MLT* is also reduced and PMI1 achieves 16% lower DC resistance compared with the non-biased STD.
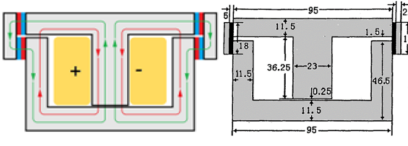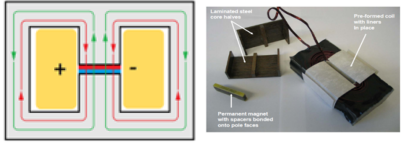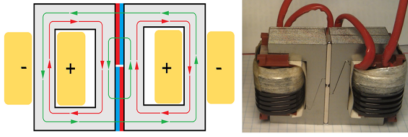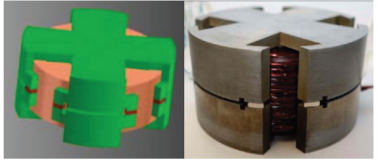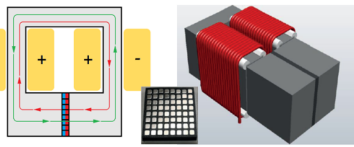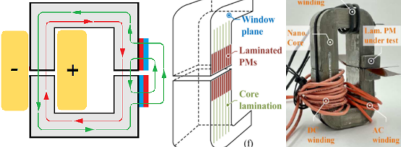
The linear part of the inductance of PMI2 has been concentrated to the operating current range, from *8A* to *10A*, resulting in an $OBIF = 3$. It also achieves 50% reduction of the core area and volume, and an additional reduction of 35% of the required number of turns, resulting in less than 50% DC resistance. Fig. 9. shows the implemented filter pairs, and their measured inductance versus current profiles, *L vs I* [21]. The latest ferrite PMBI documented in the literature was developed at MIT in 2022 [25], employing the topology depicted in Fig. 6(k). The prototype is tested with and without the PM and achieved 45% bias flux and 45% increase in saturation current. The PMBI prototype is also compared with a non-biased

pot-core with the same inductance and saturation current. The PMBI achieving a 45% bias flux, employs the associated $BIF = 1.45$, to reduce 27% the required number of turns, resulting in 50% reduction of DC resistance. Fig. 10 shows the implemented PMBI, the non-biased reference prototypes, and their measured inductance vs current profiles. The prototypes operate on a converter at 1 MHz switching frequency. The expected DC and AC ripple current, during operation, have not been specified. The authors indicate that the prototype is oriented to applications dominated by DC losses, presenting relatively low AC current ripple, $I_{DC} \gg I_{PP}$. The prototype employs a shield-ring to reduce the eddy current losses [25].

B. PMBI IMPLEMENTATIONS USING SILICON-IRON AND OTHER HIGH SATURATION CORE MATERIALS

Silicon-Iron, SiFe laminations, and other ferromagnetic core materials characterized by a high saturation flux density, B_{sat}, present a bigger challenge for practical PMBI implementation. The higher saturation limit, B_{sat} implies a higher demand for PM's bias flux, $\phi_{bias} = A_c B_{sat}$. Only six different physical PMBI implementations have been documented, using SiFe cores or other core materials with high saturation, $B_{sat} > 1T$ [6], [8], [15], [17], [23], [26]. Table IV present a summary of the different PMBI implementations, the topology employed, the materials and electrical characteristics, and their achieved bias flux, *BFI*, and overall design benefits. The first PMBI implementation using SiFe laminations core was documented

TABLE 4. Physical PMBI Implementations Using High Saturation Core Materials

Ref. Nr.	Publication Title PMBI Topology / Implementation	Year	Core material	PM material	Electrical Specifications		Bias % $BIF = \frac{B_{bias}+B_{sat}}{B_{sat}}$	Design Strategy Achievements
[6]	"The principle and design of the permanent magnet bias DC reactor"	2001	SiFe Laminations Bsat 1.2 T ρ <5 mΩ-cm μr 4000	Sintered NdFeB Br 1.2 T ρ 150 μΩ-cm μr 1	Frq Not Specified L 10 mH IDC 18 A Ipp Not specified		Not Specified ≈ 20% $BIF ≈ 1.2$	Comparison with the same inductor without PMs. 30% higher inductance at saturation current.
[8]	"Design of a high-temperature pre-biased line choke for power electronics applications"	2008	SiFe Laminations Bsat 1.6 T ρ <5 mΩ-cm μr 4000	Sintered SmCo Br 1 T ρ 100 μΩ-cm μr 1	Frq 10 kHz L 1 mH IDC 32 A Ipp 3.2 A		50% $BIF = 1.5$	Comparison with equivalent inductance and saturation current. 30% less core volume. 10% less total volume. Equivalent DC resistance.
[15]	"Size Reduction of a DC link Choke Using Saturation-gap and Biasing with Permanent Magnets"	2014	SiFe Laminations Bsat 1.5 T ρ <5 mΩ-cm μr 4000	Sintered NdFeB N42 Br 1.2 T ρ 150 μΩ-cm μr 1.1	Frq 300 Hz L 1 mH IDC 20 A Ipp 15 A		100% $BIF = 2$	Two UI PMBIs in series compared to one standard EE with equivalent inductance and saturation current. 50% smaller core volume. 30% higher DC resistance. 37% total volume reduction.
[17]	"Magnetically biased inductor for an aerospace switched reluctance drive"	2015	Somaloy (Hoganas AS) Bsat 2 T ρ > 30 Ω-cm μr 430	Sintered NdFeB Br 1 T ρ 150 μΩ-cm μr 1	Frq 100Hz-1kHz L 20 mH IDC 3.7 A Ipp 2.3 A		Not Specified ≈ 10% $BIF ≈ 1.1$	Comparison with the same inductor without PMs. 10% higher inductance.
[23]	"Premagnetization of High-Power Low-Frequency DC-Inductors in Power Electronic Applications"	2019	SiFe Laminations Bsat 1.8 T ρ <5 mΩ-cm μr 4000	Sintered NdFeB Br 1.13 T ρ 180 μΩ-cm μr 1	Frq Not specified L 1.3 mH IDC 60 A Ipp Not specified		75% $BIF = 1.75$	Compared with equivalent inductance and saturation current. 35% less number of turns. 35% lower DC resistance. Aprox. 10% smaller core volume.
[26]	"Laminated Permanent Magnets Enable Compact Magnetic Components in Current-Source"	2022	Finemet F3CC0125 Bsat 1.2 T ρ 120 Ω-cm μr 70000	Laminated NdFeB N42 Br 1.2 T ρ Not specified μr ≈1 1 mm lamination thickness	Frq 18 kHz L Not specified IDC Not specified Ipp Not specified BDC 0.6 T Bpp 0.4 T BPM 0.5 T		30% $BIF = 1.3$	Comparison between relative possitions of PMs and laminations. Laminated PMs achive 90% reduction in eddy current losses compared to standard sintered PMs.

in 2001 [6]. This prototype was the first implementation of a topology with the PMs outside the airgaps, in Fig. 5(h). The maximum PM area in this topology is also limited by the core's cross-sectional area, $A_{PM} \leq A_c$. It uses small guiding plates to contain the flux between the back of the PMs.

Unfortunately, the central leg of the core also presents an airgap, increasing the reluctance to load the PM and reducing the achievable bias flux. The prototype was tested with and without the PMs. The PMBI presented 20% higher inductance, indicating approximately 20% bias flux has been achieved.
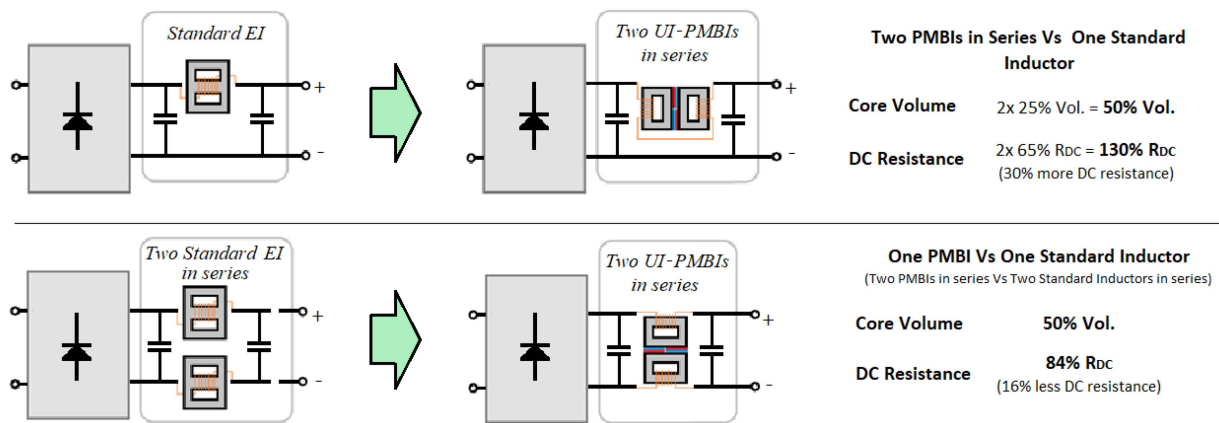
FIGURE 11. Design improvements with the *Saturation-gap* PMBI topology. 100% linear bias is achieved. *Top*: two *UI*-PMBIs in series compared with one standard non-biased *EI* inductor. *Bottom*: two *UI*-PMBIs in series compared with two standard *EI* inductors in series. Core volume and DC resistance data is empirically measured from [15] and [21].

The first implementation using SiFe cores and the basic PMBI topology with a PM inside the airgap, as in Fig. 5(a), was documented in 2008 [8]. The inductor operates at a relatively high DC current of *32 A*, and a *10 kHz* small current ripple of *3.2 A*, $I_{DC} \gg I_{PP}$. Due to its high operation temperature, it employs a sintered SmCo PM, providing better thermal performance and slightly lower remanence, B_r compared with more common NdFeB PMs. It utilizes small airgaps between the PM's poles and the edges of the core, reducing the demagnetization fields on the PM, at the expense of a lower operation point and lower achievable bias flux.

The simulated and empirically measured inductance versus current, $LvsI$ profile of this prototype is presented in [8] and Fig. 6. The achieved bias flux is 50%, resulting in a 30% core volume reduction and equivalent DC resistance. The only PMBI implementation achieving 100% biasing of a SiFe core was documented in 2014 [15], employing the *saturation-gap* topology depicted in Fig. 5(m). This topology allows for the highest PM's area compared to core's area, $A_{PM} \gg A_c$, and the PMs are in a magnetic short-circuit condition, optimizing their operation point. This topology consists of two *UU*-PMBIs, biased by the same pair of PMs. In this implementation, the two *UU*-PMBIs are connected in series, and compared to a single non-biased *EE* core inductor, achieve the same inductance and saturation current. Each *UU*-PMBI is therefore required to provide half of the total inductance. The prototype, including both *UU*-PMBIs in series, presents a 50% total core volume reduction. The total winding DC resistance of the two *UU*-PMBIs connected in series, is 30% higher compared with the single non-biased *EE* inductor. The design benefits of the *saturation-gap* topology are optimized for applications requiring a pair of DC inductors, resulting in 100% bias and reduced DC resistance, as shown in Fig. 11, and [21]. A PMBI employing a pot-core with PMs near the airgaps was documented in 2015 [17]. The allowable PM area in this topology is relatively small, limiting the achievable bias flux. The prototype was tested with and without PMs, presenting 10% higher inductance, indicating approximately

10% bias flux has been achieved. The used core material is *Somaloy*, characterized by a high saturation flux density, $B_{sat} = 2T$ and relatively low permeability, $\mu_r = 430$, resulting in a very high challenge for the PM biasing technique. A PMBI using SiFe laminations core, and the improved topology with PMs inside the airgap depicted in Fig. 5(g), was documented in 2019 [23]. The total PM area is larger than the main core's cross-sectional area, and the PM is divided into an insulated matrix of smaller PMs, increasing the achievable bias flux, and limiting demagnetization fields and eddy losses. The PMBI uses a modified UU core with single layer windings and is compared to a non-biased UU core with the same inductance and saturation current. The PMBI achieves 70% bias, and employs the *bias improvement factor, BIF=1.75* to reduce the number of turns and the required core length, like in the design strategy depicted in Fig. 2(b).

The PMBI has 35% less turns, using thicker wire cross-sectional area, and achieves a 50% reduction of the DC resistance, and approximately 10% smaller core volume. The latest PMBI implementation using a high-saturation core material was documented in 2022 [26]. This PMBI prototype employs *Finemet UU* cores and the topology with PMs near the airgap depicted in Fig. 5(j). Ideally, the *UU* cores should have only one airgap in the segment having the PMs, and no-airgap in the segment within the windings, presenting a mechanical challenge for this topology. The implemented prototype uses an airgap of *0.25 mm*, and part of the PM's flux is expected to flow through the airgap, creating a saturation-gap reluctance, like in the topology depicted in Fig. 5(l). The PMs are not in magnetic short-circuit condition, limiting their operation point and achieving a 30% bias flux. This study focused on the performance analysis of common sintered NdFeB PMs, compared with specially manufactured laminated NdFeB PMs, offering a great increase of resistivity and a good remanence. The laminated PMs achieve a 90% reduction in eddy current losses, compared with common sintered PMs. The relative alignment of the PMs and the core's laminations is also analyzed. The highest bias flux is achieved when the

PMs area is in direct contact with all the laminations, avoiding the increased reluctance between laminations.

V. CHALLENGES AND PERSPECTIVES

This section summarizes the present main challenges associated with the implementation of PMBIs, and the future perspectives of the PM biasing technique and its possible applications.

A. FURTHER EVOLUTION OF PMBI TOPOLOGIES

The *Saturation-gap*, as depicted in Fig. 5(m) and (n), provides the biggest PM's area compared to the core's cross-sectional area, $A_{PM} \gg A_c$, and presents minimal demagnetization fields on the PMs [15], [21]. The maximum area of the PMs is only limited by the length of the *UU* core, and can potentially be designed without any limitation, achieving any required bias flux level, utilizing PMs having similar resistivity as the core, as depicted in Fig. 3. This topology does not use airgaps, and the equivalent high reluctance effect is achieved by a controlled saturation of a small length within the core. This concept, using non-gapped cores with PMs, has also found further applications for the implementation of a *variable-bias inductance* operating as a *parametric transformer*, with improved efficiency and energy density compared with previous *parametric transformer* topologies [29]. This topology, employing a symmetric PM-biasing, to achieve a variable inductance, could be used for applications utilizing virtual-airgap control [105], [106]. Further evolution of the *Saturation-gap*, and other PMBI topologies, would be focused on the growing development of planar magnetics and integrated magnetics [101], [102], [103], [104].

B. MODELING AND SIMULATION OF PMBIS

While an important number of developments has been made for the modeling of the saturation and losses of common inductors [92], [93], there are relatively few developments on models for PMBIs. The mechanisms contributing to the different power losses of PMBIs can be sub-classified by:

- DC losses, R_{DC} => Winding's DC resistance.
- AC losses, Equivalent series resistance, *ESR*:
- Core losses. Including biasing effects.
- Eddy current losses in PMs.
- Skin and proximity effects losses in windings.

Winding losses in PMBIs or standard non-biased inductors, are identical in calculation. On the other hand, core losses and eddy current losses on the PMs, present additional challenges for the design of PMBIs.

All the documented implementations [5], [6], [7], [8], [9], [10], [11], [12], [13], [14], [15], [16], [17], [18], [19], [20], [21], [22], [23], [24], [25], [26] utilize simple MEC models and/or FEA simulations for design purposes. MEC models can be utilized in Spice software for circuit analysis but provide limited accuracy and are not able to predict the eddy current effects on core and PMs [11], [15]. 3D FEA simulations can achieve better accuracy than 2D FEA or MEC

simulations, as shown in [8] and Fig. 6. Nevertheless, magnetostatic FEA (2D or 3D) cannot predict eddy current effects and more complex Multiphysics FEA software is required to create PMBI models, considering temperature effects and suitable for circuit SPICE simulations. Several models have been developed for the estimation of eddy losses in PMs, operating in synchronous PM-motors [87], [87], [88], [89], which could be utilized to predict and minimize the eddy current losses in PMBIs. The curling EMF inducing the eddy currents, are proportional to the flux variations within the PM area:

$$EMF_{eddy} = -A_{eddy}\, 2\pi\, f\, \Delta B \tag{10}$$

The induced eddy current density can be estimated by:

$$J_{eddy} = \frac{EMF_{eddy}}{\rho\, l_{eddy}} \tag{11}$$

Where A_{eddy} is the area enclosed by the eddy current loop, l_{eddy} is the length of the loop, and ρ is the resistivity of the PM material. A_{eddy} and l_{eddy} are defined according to the geometrical dimensions of the PMs, and the total eddy power losses, can be estimated by integrating the infinitesimal current loops over the area of the PM [88]:

$$P_{eddy} = h_{PM} \int_0^x J_{eddy}(x)^2\, \rho\, l_{eddy}\, \partial x \tag{12}$$

Where h_{PM} is the height of the PM along its axis of magnetization. And ∂x, is the integration variable representing the distance from the minimum possible eddy current loop, at the center of the PM area, to the longest possible eddy current loop at the perimeter of the PM. These calculations only consider the flux inducing the eddy EMFs and do not account for the effects of the reaction flux. In [89] is presented a model including the effects of the reaction magnetic flux. The accurate design and loss prediction modeling is one of the present challenges for the development of PMBIs.

C. POWER LOSSES IN PMBIS

Power losses in common inductors, are typically expressed as the sum of DC and AC power losses. The DC conduction losses can be calculated by:

$$P_{DC\_Loss} = I_{DC}{}^2\, R_{DC} \tag{13}$$

And the AC losses, can be calculated by:

$$P_{AC\_Loss} = I_P{}^2\, ESR \tag{14}$$

Where R_{DC} is the DC resistance of the windings, I_{DC} is the DC current, I_P is the peak value of the AC current ripple, and *ESR* is the AC equivalent series resistance, at the operating frequency. The total losses of an inductor are highly dependent on the electrical operating conditions [93]. DC inductors operating in a relatively high DC current and a relatively small AC current ripple, $I_{DC} \gg I_{PP}$ will be dominated by DC losses (13), and the impact of the AC ESR will be minimal (14). Several PMBI implementations have achieved important reductions in DC resistance, up to 50% [13], [21], [25]. On the

other hand, only few studies documented the AC loss characteristics of the prototypes (*Equivalent series resistance, ESR or quality factor, Q*). In [7] the *Q* factor at 100kHz, of a ferrite PMBI is measured using different PM materials in the airgap. Bonded-NdFeB PMs achieve a 60% bias with only a 10% decrease in *Q* factor compared with the non-biased reference. When using sintered NdFeB PMs, the *Q* factor is reduced by an 80%, due to the low resistivity of the PMs and high eddy current losses (12). In [14] a ferrite PMBI using sintered NdFeB PMs is documented operating at 8kHz and presenting similar inductor *ESR* and converter efficiency. On the other hand, 8kHz is relatively low frequency for the ferrite core, and authors report losses increase considerably at higher frequencies, due to eddy currents on the PMs. In [15] is documented a SiFe laminations PMBI achieving 100% bias with sintered NdFeB, presenting a 10% increased *ESR* at nominal current 20A DC and a 300Hz current ripple of 7A peak. A 100% biased ferrite PMBI using bonded-NdFeB is documented in [21], presenting a 50% increase in *ESR* at 36kHz operating frequency. No more publications have documented the *ESR* or *Q* factor of the PMBI prototypes. Some authors have documented the total converter efficiency or the associated power losses and showed equivalent results when using PMBIs or standard non-biased prototypes [11], [20], [22], [25], [28]. These PMBI implementations used ferrite cores and sintered NdFeB PMs, presenting much lower resistivity than the ferrite cores, and their *ESR* values are expected to be greatly increased. Nevertheless, these converters are operating with very small current ripples, $I_P \ll I_{DC}$ (as shown in Table III) and the total losses are dominated by the DC component (13) (14), resulting in equivalent converter efficiency.

The eddy losses on the PMs are proportional to frequency and the amplitude of the flux variation (10) and inversely proportional to the PM resistivity (11). The presence of eddy currents on the PMs can increase the PMBI losses if the PM material is not adequate for the operation frequency. Topologies with the biggest PMs area in relation to the core's area, are required to achieve full bias using core and PM materials with similar resistivity, as indicated in Fig. 3. In addition of using high resistivity PM materials, other techniques have been documented oriented to reduce the eddy current losses in PMBIs. Authors in [23] employed a technique to reduce the maximum allowable eddy current loop within the PM's surface, by using a matrix of electrically insulated smaller PMs. Authors in [26] present an analysis of the eddy current loss reduction using laminated sintered PMs on a PMBI. The PMs with 1mm thick laminations, increase the PM resistance, and the eddy current losses are reduced by 90% compared with common sintered NdFeB PMs. Another more unconventional strategy for minimizing eddy current losses consists of minimizing the resistance of the eddy current loop. This strategy has been implemented using the topology depicted in Fig. 5(k) [25]. A copper shield and ring are introduced between the ferrite and the Hiperco-50 plates. Since the copper ring presents the lowest resistance, the induced eddy currents will be concentrated in the copper ring, and the total dissipated
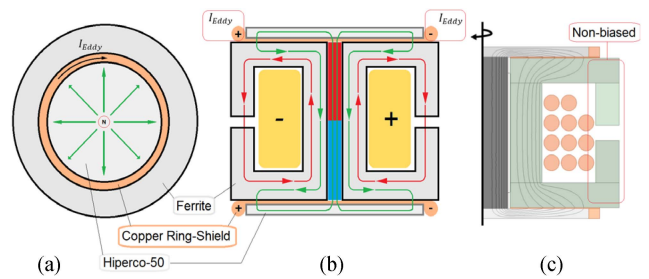

FIGURE 12. Eddy losses reduction using a copper shield-ring on pot-core. Topology depicted in Fig. 5(k). Subfigures: (a) top view, (b) cross-section side view, and (c) axisymmetric cross-section view, PM's flux simulated with FEA. Figure in (c) from [25].

eddy losses will be low (12). Fig. 12 presents a schematic representation of the shield-ring technique employed in [25]. Since the impedance of the copper ring is dependent on frequency, it is expected that the eddy current losses reduction achieved by this shield-ring should be frequency-dependent, as shown in [89]. No information about losses or the frequency performance of the shield-ring are provided in [25], [28].

The bias magnetization in the PMBI cores also modifies the mechanisms associated with core losses. The complex permeability of Mn-Zn ferrite cores has been analyzed under different levels of magnetic fields induced by external PM. The results indicate that at higher levels of magnetization, the frequency threshold of increased core losses can be extended [94], [95]. Similarly, patent [30], describes a high-frequency inductor, where external PMs introduce a bias magnetization, with the purpose of extending the usable frequency bandwidth.

D. EVALUATION OF PM DEMAGNETIZATION

Other additional challenge for the reliability of PMBIs is the evaluation and prediction of the operation point of the PMs considering its thermal effects, to guaranty operation within its linear range, avoiding the demagnetization threshold, H_k (or B_k), as depicted in Fig. 4. Approximate estimation of the PMs operation point can be obtained using MEC modeling, as depicted in Fig. 5(o), (p) and (q). PMBIs using PMs inside the airgap (Fig. 5(o)) will present a stronger demagnetization field, since most of the coil's flux is crossing through the PM's area, except for a smaller portion of fringe flux around the PM. On the other hand, PMBIs using topologies with PMs outside the airgaps or the saturation-gap topology, provides an additional path for the coil's flux, and will present smaller demagnetization fields on the PMs, as shown in the MEC models in Fig. 5(p) and (q).

Only two of the PMBI implementation documented in the literature have provided analysis and simulations to verify the operation point of the PMs to evaluate the risk of demagnetization [20], [21]. Both publications employ FEA simulations to predict the operation point of the PMs, by computing either the H field or the B field, at current levels above saturation.
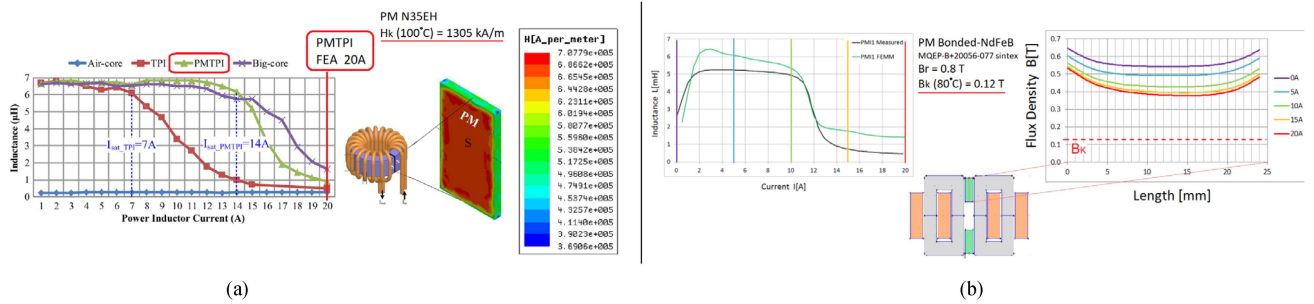
FIGURE 13. Analysis and simulation of PM demagnetization risk. (a) Toroid with PM in airgap PMTPI [20], measured inductance vs current profile, *L vs I* of different inductor prototypes, and FEA simulation of normal demagnetization field H_d on the PM of PMTPI at 20A current. (b) PMBI using saturation-gap, PMI1 [21], measured and simulated inductance vs current profile, *L vs I*, and FEA simulation of the PM flux density, *B* (*defining its operation point*) at different currents.

Fig. 13(a) and (b) presents the *L vs I* profiles and FEA simulation results of the PMBIs documented in Table III [20], [21]. Both PMBIs use ferrite cores and achieve 100% linear bias. Authors in [20] utilize a gapped ferrite toroid with a sintered NdFeB PM inserted in the airgap. The magnet grade is N35EH, providing one of the highest demagnetization thresholds available on the market (H_k 100°C=1305 kA/m). Despite the strong demagnetization fields produced in topologies with PMs inside the airgap, the employed NdFeB grade is able to resist the demagnetization field (707 kA/m) simulated at current of 20A, at which the core is in full saturation. In Fig. 13(b) is shown the measured and simulated *L vs I* profiles of the PMBI documented in [21] (PMI1). It utilizes bonded-NdFeB PMs with remanent flux density, $B_r = 0.8\ T$ and a demagnetization flux density threshold, $B_k = 0.12\ T$. The flux density through the length of the PM is simulated at several winding currents from 0A to 20A, at which the core is fully saturated. Due to the relative position of the PMs outside the coil's flux path, the demagnetization fields are smaller than topologies with PMs inside the airgap, and therefore the operation point of the PMs in the saturation-gap topology is well above the demagnetization threshold, B_k for all tested currents.

VI. CONCLUSION

This paper presents a review of the state of the art in the field of *permanent magnet biased inductors*, PMBIs. The associated design advantages, and the evolution and main characteristics of the different PMBI topologies are presented. An ideal 100% biased PMBI would provide the same inductance and saturation current as a standard DC inductor, while only requiring 50% of core's cross-sectional area, or 50% number of turns. The practical achievements of the documented PMBI prototype implementations, have been evaluated and summarized. Only the *Saturation-gap* topology, has proven to practically achieve 100% linear bias of *silicon-iron*, SiFe cores, optimizing the achievable benefits of PM biasing. *Pre-saturated* or *over-biased*, >100% linear bias levels, have been demonstrated in ferrite cores, allowing for a *bias improvement factor* higher than two, *BIF* > 2, and its associated enhanced design benefits. In DC-DC converter applications, operating with relatively high DC current and relatively small current

ripple, the employment of over-biased PMBIs, presents important advantages, potentially achieving volume reductions higher than 50%. The main challenges for the development of PMBI and one of the focuses for future work, rely on the improvement of PMBI component models for circuit simulation and prediction and minimization of eddy losses on the PMs. The combination of PMBIs with high frequency planar magnetics and integrated component design could be one of the future main trends of the PMBI technology.

REFERENCES

[1] J. T. Ludwig, "Design of optimum inductors using magnetically hard ferrites in combination with magnetically soft materials," *J. Appl. Phys.*, vol. 29, no. 3, pp. 497–499, Mar. 1958.

[2] J. T. Ludwig, "Inductors biased with permanent magnets. Part I: Theory and analysis," *Trans. Amer. Inst. Elect. Engineers, Part I: Commun. Electron.*, vol. 79, no. 3, pp. 273–278, Jul. 1960.

[3] J. T. Ludwig, "Inductors biased with permanent magnets. Part II: Design and synthesis," *Trans. Amer. Inst. Elect. Engineers, Part I: Commun. Electron.*, vol. 79, no. 3, pp. 278–291, Jul. 1960.

[4] J. T. Ludwig, "Inductors biased with permanent magnets," *Elect. Eng.*, vol. 80, no. 6, Jun. 1961, Art. no. 408.

[5] A. Nakamura and J. Ohta, "A new reverse-biased choke coil," in *Proc. Powercon 9 C-5*, TDK-Electron. Co. Ltd. Power Concepts, Inc., Jul. 1982, pp. 1–7.

[6] K. Baoquan, S. Liwei, Z. Qianfan, and C. Shukang, "The principle and design of the permanent magnet bias DC reactor," in *Proc. IEEE 5th Int. Conf. Elect. Machines Syst.*, 2001, vol. 1, pp. 230–232.

[7] T. Fujiwara and H. Matsumoto, "A new downsized large current choke coil with magnet bias method," in *Proc. 25th Int. Telecommun. Energy Conf., 2003*, Oct. 2003, pp. 416–420.

[8] R. Wrobel, N. McNeill, and P. H. Mellor, "Design of a high-temperature pre-biased line choke for power electronics applications," in *Proc. IEEE Power Electron. Specialists Conf.*, Jun. 2008, pp. 3171–3177.

[9] G. M. Shane and S. D. Sudhoff, "Permanent magnet inductor design," in *Proc. IEEE Electric Ship Technol. Symp.*, Apr. 2011, pp. 330–333.

[10] G. M. Shane and S. D. Sudhoff, "Design and optimization of permanent magnet inductors," in *2012 IEEE 27th Annu. Appl. Power Electron. Conf. Expo.*, Feb. 2012, pp. 1770–1777.

[11] G. M. Shane and S. D. Sudhoff, "Design paradigm for permanent magnet-inductor-based power converters," *IEEE Trans. Energy Convers.*, vol. 28, no. 4, pp. 880–893, Dec. 2013.

[12] Z. Dang and J. A. A. Qahouq, "Permanent magnet toroid power inductor with increased saturation current," in *2013 IEEE 28th Annu. Appl. Power Electron. Conf. Expo.*, Mar. 2013, pp. 2624–2628.

[13] S. Herzog, A. Stadler, and C. Gulden, "MaxFlux–magnetically biased inductor," Bodo's Power Syst. Mag., pp. 30–34, Jun. 2014. [Online]. Available: http://www.bodospower.com/restricted/downloads/bp_2014_06.pdf

[14] A. R. Aguilar and S. Munk-Nielsen, "Method for introducing bias magnetization in ungaped cores: 'The saturation-gap'," in *2014 IEEE Appl. Power Electron. Conf. Expo.*, Mar. 2014, pp. 721–725.

[15] A. R. Aguilar, S. Munk-Nielsen, M. Zuccherato, and H.-J. Thougaard, "Size reduction of a DC line choke using saturation gap and biasing with permanent magnets," in *Proc. PCIM Europe 2014*, Nuremberg, Germany, May 2014, pp. 1667–1674.

[16] A. R. Aguilar and S. Munk-Nielsen, "Design analysis and simulation of magnetic biased inductors with saturation-gap," in *IEEE 2014 16th Eur. Conf. Power Electron. Appl.*, 2014, pp. 1–11.

[17] S. P. McDonald, G. J. Atkinson, R. Martin, and S. Ullah, "Magnetically biased inductor for an aerospace switched reluctance drive," in *2015 IEEE Int. Electric Machines Drives Conf.*, May 2015, pp. 1272–1278.

[18] M. Schmidhuber, R. Ludwig, M. Baumann, M. Rossa, and M. Schmeller, "Magnetically biased high power coil module," in *Proc. IEEE PCIM Europe 2015, Int. Exhib. Conf. Power Electron., Intell. Motion, Renewable Energy Energy Manage.*, May 2015, pp. 1–6.

[19] Z. Dang and J. A. Abu Qahouq, "Permanent magnet power inductor with EE core for switching power converters," in *2015 IEEE Appl. Power Electron. Conf. Expo.*, Mar. 2015, pp. 1073–1077.

[20] Z. Dang and J. A. Abu Qahouq, "Evaluation of high-current toroid power inductor with NdFeB magnet for DC–DC power converters," *IEEE Trans. Ind. Electron.*, vol. 62, no. 11, pp. 6868–6876, Nov. 2015.

[21] A. R. Aguilar and S. Munk-Nielsen, "Half size reduction of DC output filter inductors with the saturation-gap magnetic bias topology," *IEEE J. Emerg. Sel. Topics Power Electron.*, vol. 4, no. 2, pp. 382–392, Jun. 2016.

[22] Z. Dang and J. A. Abu Qahouq, "Permanent-magnet coupled power inductor for multiphase DC–DC power converters," *IEEE Trans. Ind. Electron.*, vol. 64, no. 3, pp. 1971–1981, Mar. 2017.

[23] S. Lin, J. Friebe, S. Langfermann, and M. Owzareck, "Premagnetization of high-power low-frequency DC-inductors in power electronic applications," in *IEEE PCIM Europe 2019; Int. Exhib. Conf. Power Electron., Intell. Motion, Renewable Energy Energy Manage.*, May 2019, pp. 1–7.

[24] J. Friebe, S. Lin, L. Fauth, and T. Brinker, "Premagnetized inductors in single phase dc-ac and ac-dc converters," in *2019 IEEE 15thBraz. Power Electron. Conf. 5th Southern Power Electron. Conf.*, Dec. 2019, pp. 1–6.

[25] R. S. Yang, A. B. Nadler, C. R. Sullivan, and D. J. Perreault, "Permanent magnet hybrid core inductors for high saturation capability," in *2022 IEEE 23rd Workshop Control Model. Power Electron.*, Jun. 2022, pp. 1–8.

[26] Z. An et al., "Laminated permanent magnets enable compact magnetic components in current-source converters," *IEEE Trans. Power Electron.*, vol. 37, no. 10, pp. 12391–12405, Oct. 2022.

[27] B. Houska, D. Yan, J. Benzaquen, and D. Divan, "Partial saturation in permanent magnet inductors," in *Proc. 2022 IEEE Energy Convers. Congr. Expo.*, Oct. 2022, pp. 1–7.

[28] R. S. Yang, A. B. Nadler, C. R. Sullivan, and D. J. Perreault, "Permanent magnet hybrid core inductors for high saturation capability," *IEEE Open J. Power Electron.*, vol. 4, pp. 603–614, 2023.

[29] A. R. Aguilar, B. Rannestad, and S. Munk-Nielsen, "Parametric transformer using PM-inductors with saturation-gap," *IET Power Electron.*, vol. 13, no. 19, pp. 4581–4591, Dec. 2020, doi: 10.1049/iet-pel.2020.0846.

[30] J. M. Cluwern, "Inductor comprising a permanently premagnetized magnet core," Patent CA606140A, Oct. 04, 1960. [Online]. Available: https://worldwide.espacenet.com/patent/search/family/035827620/publication/CA606140A?q=pn%3DCA606140A

[31] R. Pieters, "Variable inductor having core saturation controlled by magnet," Patent US3359519A, Dec. 19, 1967. [Online]. Available: https://worldwide.espacenet.com/patent/search/family/019790757/publication/US3359519A?q=pn%3DUS3359519A

[32] N. Sinnott and H. Jones, "High power electrically variable inductor," Patent US3735305A, May 22, 1973. [Online]. Available: https://worldwide.espacenet.com/patent/search/family/023116747/publication/US3735305A?q=pn%3DUS3735305A

[33] F. Masahiko, "Inductor," Patent JPS5136564A, Mar. 27, 1976. [Online]. Available: https://worldwide.espacenet.com/patent/search/family/014492596/publication/JPS5136564A?q=pn%3DJPS5136564A

[34] F. Masahiko and K. Yasuji, "Inductor," Patent US4009460A, Feb. 22, 1977. [Online]. Available: https://worldwide.espacenet.com/patent/search/family/026448574/publication/US4009460A?q=pn%3DUS4009460A

[35] F. Masahiko, S. Hiromi, and O. Masao, "Inductor with plurality of magnet pieces in air gap," Patent US4103221A, Jul. 25, 1978. [Online]. Available: https://worldwide.espacenet.com/patent/search/family/027563612/publication/US4103221A?q=pn%3DUS4103221A

[36] R. Glen, "Magnetically biased inductor," Patent US4491819A, Jan. 01, 1985. [Online]. Available: https://worldwide.espacenet.com/patent/search/family/024112126/publication/US4491819A?q=pn%3DUS4491819A

[37] T. Ryuchirou, I. Noriaki, and Z. Michihiko, "D.C. reactor," Patent EP0744757A1, Nov. 27, 1996. [Online]. Available: https://worldwide.espacenet.com/patent/search/family/027303672/publication/EP0744757A1?q=pn%3DEP0744757A1

[38] T. Ryuchirou, "DC reactor," Patent JPH09213546A, Aug. 15, 1997. [Online]. Available: https://worldwide.espacenet.com/patent/search?q=pn%3DJPH09213546A

[39] W. Jialin, "Small volume high efficiency DC reactor," Patent CN2356409Y, Dec. 29, 1999. [Online]. Available: https://worldwide.espacenet.com/patent/search?q=pn%3DCN2356409Y

[40] I. Toru, "Inductor component," Patent JP2002359125A, Dec. 13, 2002. [Online]. Available: https://worldwide.espacenet.com/patent/search?q=pn%3DJP2002359125

[41] K. Masahiro, "Inductor component," Patent JP2003017340A, Jan. 17, 2003. [Online]. Available: https://worldwide.espacenet.com/patent/search?q=pn%3DJP2003017340A

[42] F. Teruhiko, "Permanent magnet magnetic core having the magnet as bias magnet and inductance parts using the core, Patent WO0221543A1, Mar. 14, 2002. [Online]. Available: https://worldwide.espacenet.com/patent/search?q=pn%3DWO0221543A1

[43] F. Teruhiko, "Magnetic core including magnet for magnetic bias and inductor component using the same," Patent US2002097126A1, Jul. 25, 2002. [Online]. Available: https://worldwide.espacenet.com/patent/search?q=pn%3DUS2002097126A1

[44] O. Kazuyuki, "Inductor component having a permanent magnet in the vicinity of magnetic gap," Patent US2002089400A1, Jul. 11, 2002. [Online]. Available: https://worldwide.espacenet.com/patent/search?q=pn%3DUS2002089400A1

[45] K. Masahiro, "Inductor component," Patent JP2002289443A, Oct. 04, 2002. [Online]. Available: https://worldwide.espacenet.com/patent/search?q=pn%3DJP2002289443A

[46] O. Kazuyuki, "Inductor component," Patent JP2002313647A, Oct. 25, 2002. [Online]. Available: https://worldwide.espacenet.com/patent/search?q=pn%3DJP2002313647A

[47] O. Kazuyuki, "Inductor," Patent JP2002222714A. Aug. 09, 2002. [Online]. Available: https://worldwide.espacenet.com/patent/search?q=pn%3DJP2002222714A

[48] S. Yoshitaka, "Stacked inductor and its manufacturing method," Patent JP2002175917A, Jun. 21, 2002. [Online]. Available: https://worldwide.espacenet.com/patent/search?q=pn%3DJP2002175917A

[49] S. Toshiya, "Inductor," Patent JP2002175925A, Jun. 21, 2002. [Online]. Available: https://worldwide.espacenet.com/patent/search?q=pn%3DJP2002175925A

[50] T. Yoshihiro, "DC reactor," Patent JP2003318046A, Nov. 07, 2003. [Online]. Available: https://worldwide.espacenet.com/patent/search?q=pn%3DJP2003318046A

[51] N. Akinori, "DC reactor," Patent JP2004055734A, Feb. 19, 2004. [Online]. Available: https://worldwide.espacenet.com/patent/search?q=pn%3DJP2004055734A

[52] K. Masahiro, "Inductor part," Patent JP2003124041A, Apr. 25, 2003. [Online]. Available: https://worldwide.espacenet.com/patent/search?q=pn%3DJP2003124041A

[53] I. Toshiyuki, "DC reactor," Patent JP2004055787A, Feb. 19, 2004. [Online]. Available: https://worldwide.espacenet.com/patent/search?q=pn%3DJP2004055787A

[54] K. Mitsutsugu, "Laminate inductor," Patent JP2006196591A, Jul. 27, 2006. [Online]. Available: https://worldwide.espacenet.com/patent/search?q=pn%3DJP2006196591A

[55] T. Ryuchiro, "DC reactor," Patent JP3765326B2, Apr. 12, 2006. [Online]. Available: https://worldwide.espacenet.com/patent/search?q=pn%3DJP3765326B2

[56] F. Teruhiko, "Magnetically biasing bond magnet for improving DC superposition characteristics of magnetic coil," Patent US6995643B2, Feb. 07, 2006. [Online]. Available: https://worldwide.espacenet.com/patent/search?q=pn%3DUS6995643B2

[57] K. Mitsugu, "Inductor," Patent US2006214759A1, Sep. 28, 2006. [Online]. Available: https://worldwide.espacenet.com/patent/search?q=pn%3DUS2006214759A1

[58] T. Mean-Jue, "Monolithic inductor," Patent TW200828356A, Jul. 01, 2008. [Online]. Available: https://worldwide.espacenet.com/patent/search?q=pn%3DTW200828356A

[59] I. Toshiyuki, "DC reactor," Patent JP2007281204A, Oct. 25, 2007. [Online]. Available: https://worldwide.espacenet.com/patent/search?q=pn%3DJP2007281204A

[60] V. Tero, "DC inductor," Patent EP2001029A1, Dec. 10, 2008. [Online]. Available: https://worldwide.espacenet.com/patent/search?q=pn%3DEP2001029A1

[61] K. Masahiro, "Inductor," Patent JP2008078177A, Apr. 03, 2008. [Online]. Available: https://worldwide.espacenet.com/patent/search?q=pn%3DJP2008078177A

[62] V. Tero, "DC inductor," Patent US2008303620A1, Dec. 11, 2008. [Online]. Available: https://worldwide.espacenet.com/patent/search?q=pn%3DUS2008303620A1

[63] V. Tero, "Protection of permanent magnets in a DC inductor," Patent US2008303619A1, Dec. 11, 2008. [Online]. Available: https://worldwide.espacenet.com/patent/search?q=pn%3DUS2008303619A1

[64] T. Hansen, "High powered inductors using a magnetic basis," Patent US2009066454A1, Mar. 12, 2009. [Online]. Available: https://worldwide.espacenet.com/patent/search?q=pn%3DUS2008303619A1

[65] P. Paulilus, "Permanent magnet DC inductor," Patent EP2216794A1, Aug. 11, 2010. [Online]. Available: https://worldwide.espacenet.com/patent/search?q=pn%3DEP2216794A1

[66] W. Jiaju, "Inductance element provided with permanent magnet bias magnet and bypass magnetic core," Patent CN103578688A, Feb. 12, 2014. [Online]. Available: https://worldwide.espacenet.com/patent/search?q=pn%3DCN103578688A

[67] M. Daisuke, "Multilayer inductor," Patent JP2015198159A, Nov. 09, 2015. [Online]. Available: https://worldwide.espacenet.com/patent/search?q=pn%3DJP2015198159A

[68] G. Christof, "Magnetically biased choke," Patent US2016042855A1, May 02, 2014. [Online]. Available: https://worldwide.espacenet.com/patent/search?q=pn%3DUS2016042855A1

[69] C. Wei, "Permanent magnet biased magnetic element assembly and method for implementing same," Patent CN106057395A, Oct. 26, 2016. [Online]. Available: https://worldwide.espacenet.com/patent/search?q=pn%3DCN106057395A

[70] J. A. Qahouq, "Multi-stage permanent magnet structure and integrated power inductors," Patent US2017117077A1, Apr. 27, 2017. [Online]. Available: https://worldwide.espacenet.com/patent/search?q=pn%3DUS2017117077A1

[71] L. Minmin, "High-saturation-current integrated inductor," Patent CN212136108U, Dec. 11, 2020. [Online]. Available: https://worldwide.espacenet.com/patent/search?q=pn%3DCN212136108U

[72] C. Xin, "Power inductor," Patent CN212136185U, Dec. 11, 2020. [Online]. Available: https://worldwide.espacenet.com/patent/search?q=pn%3DCN212136185U

[73] N. Sturcken, "Apparatus and methods for magnetic core inductors with biased permeability," Patent US10629357B2, Mar. 21, 2020. [Online]. Available: https://worldwide.espacenet.com/patent/search?q=pn%3DUS10629357B2

[74] L. David, "Magnetic composition and magnetic component including the same," Patent US2021249176A1, Aug. 12, 2021. [Online]. Available: https://worldwide.espacenet.com/patent/search?q=pn%3DUS2021249176A1

[75] C. McLyman, *Transformer and Inductor Design Handbook*, 4th ed. Boca Raton, FL, USA: CRC Press, 2017, doi: 10.1201/b10865.

[76] W. G. Hurley and W. H.Wölfle, *Transformers and Inductors for Power Electronics: Theory, Design and Applications*, 1st ed. Hoboken, NJ, USA: Wiley, 2013.

[77] J. W. Kolar et al., "PWM converter power density barriers," in *2007 IEEE Power Convers. Conf.*, Nagoya, Japan, 2007, pp. P-9–P-29.

[78] B. W. Williams, "Hard magnetic materials," in *Power Electronics: Devices, Drivers, Applications, and Passive Components*, New York, NY, USA: McGraw-Hill, 2006, ch. 32, pp. 1431–1469. [Online]. Available: http://personal.strath.ac.uk/barry.williams/book.htm

[79] B. Bochenkov and S. Lutz, "A review of modern materials of permanent magnets," in *Proc. IEEE 8th Russian-Korean Int. Symp. Sci.Technol.*, Tomsk, Russia, 2004, vol. 1, pp. 201–203, doi: 10.1109/KORUS.2004.1555319.

[80] U. S. Deshpande, "Recent advances in materials for use in permanent magnet machines-a review," in *Proc. IEEE Int. Electric Machines Drives Conf.*, Madison, WI, USA, 2003, vol. 1, pp. 509–515, doi: 10.1109/IEMDC.2003.1211311.

[81] S. R. Trout, "Material selection of permanent magnets, considering thermal properties correctly," in *Proc. IEEE Elect. Insul. Conf. Elect. Manuf. Coil Winding Conf.*, Cincinnati, OH, USA, 2001, pp. 365–370, doi: 10.1109/EEIC.2001.965683.

[82] H. C. Lovatt and P. A. Watterson, "Energy stored in permanent magnets," *IEEE Trans. Magn.*, vol. 35, no. 1, pp. 505–507, Jan. 1999.

[83] J. Friebe and P. Zacharias, "Review of magnetic material degradation characteristics for the design of premagnetized inductors," *IEEE Trans. Magn.*, vol. 50, no. 3, pp. 40–48, Mar. 2014.

[84] W. Pan, W. Li, L. Y. Cui, X. M. Li, and Z. H. Guo, "Rare earth magnets resisting eddy currents," *IEEE Trans. Magn.*, vol. 35, no. 5, pp. 3343–3345, Sep. 1999, doi: 10.1109/20.800519.

[85] G. Bertotti, *Hysteresis in Magnetism*, 1st ed. San Diego, CA, USA: Academic, May 1998.

[86] A. Kalimov, F. Klos, B. Langenbeck, and G. Moritz, "Dynamic processes in laminated magnets: Simulation and comparison with experimental results," *IEEE Trans. Appl. Supercond.*, vol. 12, no. 1, pp. 98–101, Mar. 2002, doi: 10.1109/TASC.2002.1018360.

[87] M. Hullmann and B. Ponick, "General analytical description of the effects of segmentation on eddy current losses in rectangular magnets," in *Proc. IEEE 2022 Int. Conf. Elect. Machines*, Valencia, Spain, 2022, pp. 1757–1762, doi: 10.1109/ICEM51905.2022.9910629.

[88] S. Ruoho, T. Santa-Nokki, J. Kolehmainen, and A. Arkkio, "Modeling magnet length in 2-D finite-element analysis of electric machines," *IEEE Trans. Magn.*, vol. 45, no. 8, pp. 3114–3120, Aug. 2009, doi: 10.1109/TMAG.2009.2018621.

[89] M. Königs and B. Löhlein, "Lumped model for the calculation of harmonic eddy current losses in permanent magnets for homogeneous flux distributions considering eddy current reaction flux," *Elektrotech. Inftech.*, vol. 140, pp. 488–496, 2023.

[90] G. Ouyang, X. Chen, Y. Liang, C. Macziewski, and J. Cui, "Review of Fe-6.5wt%Si high silicon steel - A promising soft magnetic material for sub-kHz application," *J. Magnetism Magn. Mater.*, vol. 481, pp. 234–250, Jul. 2019.

[91] F. Fiorillo, G. Bertotti, C. Appino, and M. Pasquale, "Soft magnetic materials," in *Wiley Encyclopedia of Electrical and Electronics Engineering*. New York, NY, United States: Wiley, Nov. 2016.

[92] D. Rodriguez-Sotelo et al., "Power losses models for magnetic cores: A review," *Micromachines*, vol. 13, no. 3, Mar. 2022, Art. no. 418, doi: 10.3390/mi13030418.

[93] R. J. Pasterczyk and T. Delaforge, "Engineering illusion to accurately predict power losses in magnetic materials on the base of standard manufacturers' datasheets," in *Proc. IEEE. PCIM Europe 2014; Int. Exhib. Conf. Power Electron., Intell. Motion, Renewable Energy Energy Manage.*, Nuremberg, Germany, May 2014, pp. 1–9.

[94] T. Tsutaoka et al., "Magnetic field effect on the complex permeability for a Mn–Zn ferrite and its composite materials," *J. Eur. Ceram. Soc.*, vol. 19, pp. 1531–1535, 1999.

[95] T. P. Todorova, "Control of N87 Mn-Zn ferrite permeability using externally applied static magnetic field," in *2023 IEEE XXXII Int. Sci. Conf. Electron.*, Sozopol, Bulgaria, 2023, pp. 1–5, doi: 10.1109/ET59121.2023.10278596.

[96] J. Muhlethaler, J. Biela, J. W. Kolar, and A. Ecklebe, "Core losses under the DC bias condition based on Steinmetz parameters," *IEEE Trans. Power Electron.*, vol. 27, no. 2, pp. 953–963, Feb. 2012, doi: 10.1109/TPEL.2011.2160971.

[97] H. Kosai, Z. Turgut, and J. Scofield, "Experimental investigation of DC-bias related core losses in a boost inductor," *IEEE Trans. Magn.*, vol. 49, no. 7, pp. 4168–4171, Jul. 2013, doi: 10.1109/TMAG.2013.2242863.

[98] P. Herget et al., "A study of current density limits due to saturation in thin film magnetic inductors for on-chip power conversion," *IEEE Trans. Magn.*, vol. 48, no. 11, pp. 4119–4122, Nov. 2012, doi: 10.1109/TMAG.2012.2201140.

[99] H. Zhao et al., "Physics-based modeling of parasitic capacitance in medium-voltage filter inductors," *IEEE Trans. Power Electron.*, vol. 36, no. 1, pp. 829–843, Jan. 2021, doi: 10.1109/TPEL.2020.3003157.

[100] C. Feeney, M. Duffy, N. Wang, and C. O'Mathuna, "Advantages of paralleling inductors-on-silicon in high frequency power converters," in *2013 IEEE 28th Annu. Appl. Power Electron. Conf. Expo.*, Long Beach, CA, USA, 2013, pp. 686–691, doi: 10.1109/APEC.2013.6520284.

[101] S. O'Reilly, M. Duffy, T. O'Donnell, P. McCloskey, and S. Cian Ó Mathúna, "Integrated passives in advanced printed wiring boards," *Circuit World*, vol. 27, no. 4, pp. 22–25, 2001.

[102] K.Warnakulasuriya, A. Polti, and F. Nabhani, "Evolution of magnetics in power electronics applications and facing the challenges of future electronics industry," in *Proc. IEEE PCIM Europe 2017; Int. Exhib. Conf. Power Electron., Intell. Motion, Renewable Energy Energy Manage.*, 2017, pp. 1–5.

[103] Z. Ouyang, O. C. Thomsen, and M. A. E. Andersen, "Optimal design and tradeoff analysis of planar transformer in high-power DC-DC converters," *IEEE Trans. Ind. Electron.*, vol. 59, no. 7, pp. 2800–2810, Jul. 2012.

[104] Z. Ouyang and M. A. E. Andersen, "Overview of planar magnetic technology—Fundamental properties," *IEEE Trans. Power Electron.*, vol. 29, no. 9, pp. 4888–4900, Sep. 2014.

[105] D. Sevsek, M. Hinkkanen, J. Kukkola, and M. Lehtonen, "Dynamic model of a virtual air gap reactor," *IEEE Trans. Power Del.*, vol. 38, no. 4, pp. 2521–2530, Aug. 2023, doi: 10.1109/TPWRD.2023.3245123.

[106] D. S. L. Dolan and P. W. Lehn, "Harmonic mitigation in a virtual air gap variable reactor via control current modulation," in *2008 IEEE Power Energy Soc. Gen. Meeting - Convers. Del. Elect. Energy 21st Century*, Pittsburgh, PA, USA, 2008, pp. 1–5, doi: 10.1109/PES.2008.4595983.

ANDRES REVILLA AGUILAR (Member, IEEE) received the B.Sc. degree in telecommunications engineering from the Polytechnic University of Madrid, Madrid, Spain, in 2004, and the M.Sc. degree in acoustics and the Ph.D. degree in power electronics from Aalborg University, Aalborg, Denmark, in 2006 and 2023, respectively. His research interest includes permanent magnet inductors and high-power-density magnetics for power electronics applications.

STIG MUNK-NIELSEN (Member, IEEE) received the M.Sc. and Ph.D. degrees from Aalborg University, Aalborg, Denmark, in 1991 and 1997, respectively. He is currently a Professor with AAU Energy, Aalborg University, Aalborg, Denmark. His research interests include LV and MV Si, SiC, and GaN converters, packaging of power electronic devices, electrical monitoring apparatus for IGBTs, failure modes, and device test systems. In the last ten years, he has been involved in or has managed ten research projects and has authored or coauthored 242 international power electronic papers.

FLEMMING BUUS BENDIXEN (Member, IEEE) received the M.Sc. and Ph.D. degrees from Aalborg university, Aalborg, Denmark in 1997 and 2006, respectively. Since 1999, Owner of Buus-Mag has been a Consultant Engineer in magnetic calculations for various Danish customers. He has filed more than 22 different international publications on conferences and journals and participated in more than 55 international conferences/courses within the areas motor-design, magnetism, renewable energy, motor control and power electronics. The main organizer of six international conferences in collaboration between U.K. magnetics society and Danish magnetic society.

ZIWEI OUYANG (Senior Member, IEEE) received the Ph.D. degree from the Technical University of Denmark (DTU), Kongens Lyngby, in 2011. From 2011 to 2013, he was a Postdoc Researcher with DTU. From 2013 to 2016, he was an Assistant Professor with the same department. Since 2016, he has been an Associate Professor with DTU. In November 2021, he was appointed as the Head of Study for the M.Sc. Program in electrical engineering. He has been invited to give lectures in many universities, enterprises and educational seminars and workshops around the world. He has 132 high impact IEEE journal and conference publications, co-author on a book chapter on Magnetics for the "Handbook of Power Electronics" and currently he is the holder of ten international patents. His research interests include switch mode power supply, magnetics modeling and integration, high-density high-efficiency power converters, energy storage system, and wireless charging. In 2023, he was honored by the prestigious ERC Consolidated Grant with a funding of 2 million Euros. He was the recipient of the 2021 IEEE Transactions on Power Electronics First Place Prize Paper Award. He was also the recipient of the Young Engineer Award at PCIM-Asia 2014, Best Ph.D. Dissertation of the Year Award 2012 in DTU, and several Best Paper Awards in IEEE sponsored international conferences

MAEVE DUFFY (Senior Member, IEEE) received the B.E. and Ph.D. degrees in electronic engineering from the National University of Ireland (NUI), Galway, Ireland, in 1992 and 1997, respectively. From 1997 to 2001, she was a Research Assistant with PEI Technologies, NMRC (now Tyndall National Institute), Cork, Ireland. In 2001, she returned to an academic position in electrical and electronic engineering with the University of Galway. She is currently a Professor with the School of Engineering, University of Galway, Galway. She carries out her research at the Power Electronics Research Centre. She has authored or coauthored more than 100 peer-reviewed journal articles and conference papers in the areas of magnetic component design and power electronics. Her research interests include modelling and design of power electronic components, circuits and systems for microprocessor loads, biomedical applications, energy harvesting, and wireless power systems.

HONGBO ZHAO (Member, IEEE) received the Ph.D. degree in power electronics from Aalborg University, Aalborg, Denmark, in 2021. He was a Visiting Researcher with the University of Texas at Austin, Austin, Texas, USA, Visiting Scholar with the University of Galway, Galway, Ireland, and Visiting Professor with G2Elab, Grenoble, France. He is currently an Assistant Professor with AAU Energy, Aalborg University. He has authored or coauthored around 60 peer-reviewed publications and is the first inventor for four pending international patent applications. His research interests include analysis and packaging of modern magnetic components and the applications of wide bandgap semiconductor devices. He received the Villum Fellowship in 2022. In 2023, he was the recipient of "The Bright Idea Award" from Otto Mønsteds Fond for his idea on next-generation sustainable magnetic components. In 2022, he was also the recipient of the "Best Magnetic Design" by Frenetic. He was selected as a future entrepreneur by the Spin-outs Denmark program in 2023.